Article

Structure of *Tetrahymena* telomerase-bound CST with polymerase α-primase

https://doi.org/10.1038/s41586-022-04931-7

Received: 29 December 2021

Accepted: 6 June 2022

Published online: 13 July 2022

Check for updates

Yao He[1,2,4], He Song[1,4], Henry Chan[1], Baocheng Liu[1], Yaqiang Wang[1], Lukas Sušac[1], Z. Hong Zhou[2,3] & Juli Feigon[1]✉

Telomeres are the physical ends of linear chromosomes. They are composed of short repeating sequences (such as TTGGGG in the G-strand for *Tetrahymena thermophila*) of double-stranded DNA with a single-strand 3′ overhang of the G-strand and, in humans, the six shelterin proteins: TPP1, POT1, TRF1, TRF2, RAP1 and TIN2[1,2]. TPP1 and POT1 associate with the 3′ overhang, with POT1 binding the G-strand[3] and TPP1 (in complex with TIN2[4]) recruiting telomerase via interaction with telomerase reverse transcriptase[5] (TERT). The telomere DNA ends are replicated and maintained by telomerase[6], for the G-strand, and subsequently DNA polymerase α–primase[7,8] (PolαPrim), for the C-strand[9]. PolαPrim activity is stimulated by the heterotrimeric complex CTC1–STN1–TEN1[10–12] (CST), but the structural basis of the recruitment of PolαPrim and CST to telomere ends remains unknown. Here we report cryo-electron microscopy (cryo-EM) structures of *Tetrahymena* CST in the context of the telomerase holoenzyme, in both the absence and the presence of PolαPrim, and of PolαPrim alone. *Tetrahymena* Ctc1 binds telomerase subunit p50, a TPP1 orthologue, on a flexible Ctc1 binding motif revealed by cryo-EM and NMR spectroscopy. The PolαPrim polymerase subunit POLA1 binds Ctc1 and Stn1, and its interface with Ctc1 forms an entry port for G-strand DNA to the POLA1 active site. We thus provide a snapshot of four key components that are required for telomeric DNA synthesis in a single active complex—telomerase-core ribonucleoprotein, p50, CST and PolαPrim—that provides insights into the recruitment of CST and PolαPrim and the handoff between G-strand and C-strand synthesis.

Synthesis of the G-strand at the ends of telomeres by telomerase is terminated by CST[12,13]. Human CST is essential for maintaining the telomere C-strand and also has a role in overcoming genome-wide replication stress[10,14,15]. Similar to the shelterin proteins and telomerase, mutations in human CST lead to telomere biology disorders[16] including Coats plus syndrome and dyskeratosis congenita[17]. The CST small subunits STN1 and TEN1 are structurally homologous to those in replication protein A[18] (RPA), a single-stranded DNA-binding protein that is involved in all aspects of DNA replication and repair, whereas the large subunit—Ctc1 in *Tetrahymena*, CTC1 in vertebrates and Cdc13 in yeast—is more diverse[19–23]. Structural and biochemical studies of CST proteins have suggested various stoichiometries, oligomerization states and functions of subunits[19,20,23]. The structure of complete CST[19] from human revealed a decameric architecture of heterotrimers in the presence of single-stranded telomeric (G-strand) DNA (sstDNA). In vertebrates, CST is proposed to inhibit telomerase activity by physically interacting with the shelterin proteins TPP1 or POT1 at telomere ends[12,24,25] and G-strand sequestration[12,13], and it promotes C-strand fill-in by association with PolαPrim[26–29], but there is a lack of structures of these interactions from any organism. PolαPrim is an unusual polymerase containing both primase and DNA polymerase subunits; the primase synthesizes an RNA primer on a DNA template and then hands off the RNA primer–DNA template to the DNA polymerase, which initiates synthesis of a short DNA duplex[7,8]. PolαPrim initiates the synthesis of both the leading and the lagging strands in eukaryotes[8] and, in association with CST, has functions in genome-wide DNA repair[15] in addition to its role in C-strand synthesis at telomere ends.

The *Tetrahymena* telomerase holoenzyme comprises—in addition to its catalytic-core ribonucleoprotein (RNP) of TERT, telomerase RNA (TER), which provides the template for G-strand telomere-repeat synthesis, and LARP7 assembly protein p65—a set of proteins that are orthologous to human proteins that only transiently associate with telomerase at telomeres[30]. These include p50, the structural and functional equivalent of TPP1, which recruits and activates telomerase[22,31–33]; Teb1, a subunit of the trimeric RPA-related complex TEB[22,34], which binds the sstDNA[35] and together with p50 increases telomerase activity and processivity, similar to its orthologue POT1[36–38]; and another trimeric RPA-related complex p75–p45–p19, which has been identified as *Tetrahymena* Ctc1–Stn1–Ten1[22,23] (TtCST). The constitutive association of these proteins with the telomerase catalytic core makes *Tetrahymena*

[1]Department of Chemistry and Biochemistry, University of California, Los Angeles, Los Angeles, CA, USA. [2]Department of Microbiology, Immunology, and Molecular Genetics, University of California, Los Angeles, Los Angeles, CA, USA. [3]California NanoSystems Institute, University of California, Los Angeles, Los Angeles, CA, USA. [4]These authors contributed equally: Yao He, He Song. ✉e-mail: feigon@mbi.ucla.edu

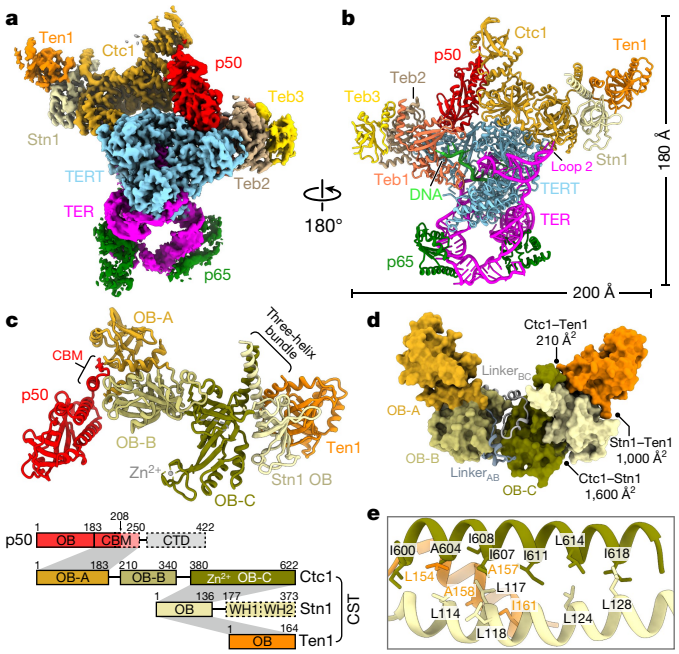

Fig. 1 | Cryo-EM structure of TtCST in the telomerase holoenzyme. **a**, Cryo-EM map of the telomerase holoenzyme. **b**, Ribbon representation of the model of telomerase holoenzyme, rotated 180° relative to **a**. The proteins, TER and DNA are colour-coded as indicated. **c**, Structure and schematic of TtCST with p50. The three OB domains (OB-A, OB-B and OB-C) of Ctc1 are coloured individually as indicated. In the schematic, regions that are not visible in the cryo-EM map are shown as dashed boxes and intermolecular interactions between proteins are indicated with grey shading. OB, oligonucleotide/oligosaccharide-binding fold domain; WH, winged-helix domain; CBM, Ctc1 binding motif; CTD, C-terminal domain; Zn^{2+}, zinc ribbon motif. **d**, Surface representation of the TtCST structure. Buried surface areas in the interfaces between TtCST subunits are indicated. The two structured linkers between the Ctc1 OB domains are shown as ribbon. **e**, Close-up view of the hydrophobic interface of the TtCST intermolecular three-helix bundle.

telomerase an ideal model system for elucidating details of the protein structures and interactions that regulate G-strand and C-strand synthesis[22,39,40]. Here we report structural and functional studies of *Tetrahymena* telomerase and PolαPrim that show how monomeric TtCST binds p50 and PolαPrim on different interfaces to coordinate G-strand termination and C-strand fill-in synthesis, and suggest commonalities with interactions at human telomeres.

Structure of *Tetrahymena* telomerase CST

Although cryo-EM studies of *Tetrahymena* telomerase have provided high-resolution structures of the catalytic-core RNP, TEB heterotrimer and the oligonucleotide/oligosaccharide-binding fold (OB) domain of p50 (ref. [40]), the dynamic positioning of TtCST has limited modelling of its structure. Here we combined three previously reported datasets of *Tetrahymena* telomerase bound to sstDNA[40] and performed focused classification on TtCST followed by refinement of the holoenzyme to obtain a reconstruction with an overall resolution of 3.5 Å (Fig. 1a, Extended Data Fig. 1 and Extended Data Table 1). For the model of TtCST, Stn1–Ten1 crystal structures[22,23] were rigid-body fit into the density and manually refined with little change, and Ctc1 was built de novo (Fig. 1b and Extended Data Fig. 2). Modelling of the N-terminal domain of Ctc1, which has lower resolution (Extended Data Fig. 1c), was facilitated by using information derived from NMR data on secondary structure elements and inter-β-strand nuclear Overhauser effects (NOEs) (Methods) (Extended Data Fig. 3). Ctc1, whose domain structure was not previously established, comprises three OB domains (OB-A, OB-B and OB-C) connected by structured linkers that stabilize the rigid pairwise interactions between the domains (Fig. 1c,d). Ctc1 OB-C has a C-shaped cleft and zinc ribbon motif (Fig. 1c) typical of the C-terminal OB domain of the large subunit of RPA[18] and related complexes, including mammalian CTC1[19], POT1[37,38] and *Tetrahymena* Teb1[35,40]. Ctc1 OB-C forms a heterotrimer with the Stn1 OB and Ten1 OB domains that is stabilized by an intermolecular three-helix bundle (Fig. 1c,e) and by Ten1–Stn1 and Stn1–Ctc1 OB-domain interactions (Extended Data Fig. 2c–h). The tandem winged helix-turn-helix (WH–WH) domain of Stn1 is connected to its OB domain by a flexible linker and is not visible in the cryo-EM map, consistent with its multi-positioning shown by negative-stain electron microscopy[22]. Overall, this structure of monomeric TtCST strongly suggests its origin from RPA and establishes the domain structure of the least conserved subunit Ctc1.

Flexible interface between Ctc1 and p50

p50 has an N-terminal OB domain and a C-terminal domain that is not visible in the cryo-EM map (Fig. 1a). The p50 OB and human TPP1 OB domains interact with telomerase on TERT TEN and TRAP domains[32,33,39–42], but how *Tetrahymena* p50, human TPP1 or mouse POT1 interacts with CST is unknown[24,25]. We find that TtCST is anchored on p50 via Ctc1 OB-A (Fig. 1c). In the structure, TtCST is positioned across the top of the TERT ring (Fig. 1b) and stabilized in this predominant conformation by additional interactions between Ctc1 and the TERT–TER catalytic core (Extended Data Fig. 2j–l). However, these are not stable interactions, as other conformations resolved by 3D classification show TtCST hinged away from TERT (Fig. 2a and Extended Data Fig. 1a). In the cryo-EM map, a previously uncharacterized density of p50 protrudes from the C terminus of its OB domain into Ctc1 OB-A (Extended Data Fig. 1h). p50 residues 185–208 were built against the density as helix α5 and strand β7, the latter of which forms an extended β sheet with β1–β4–β5′ of Ctc1 OB-A (Fig. 2b). However, previous biochemical studies have shown that p50 C-terminal truncation at residue 213 almost abrogates binding with Ctc1, whereas truncation at residue 252 binds to Ctc1 comparably to the full-length protein[43]. We therefore investigated whether p50 residues between 208–255 contribute to the binding interface with Ctc1. We made a series of p50 peptides and monitored their interaction with Ctc1 OB-A by NMR (Extended Data Fig. 4). ^{1}H-^{15}N heteronuclear single quantum coherence spectroscopy (HSQC) spectra show that optimal binding requires residues 228–250 (Fig. 2c and Extended Data Fig. 4b). This peptide forms a 1:1 complex with Ctc1 OB-A that is in slow exchange on the NMR timescale, indicating a slow off-rate (Extended Data Fig. 4c). Talos+ secondary structure scores, CS-Rosetta modelling and chemical shift mapping (Methods) indicate that p50 peptide residues 228–241 form a β-hairpin that interacts with the Ctc1 OB-A β-barrel near the β1–β2 linker, β4 and β5 (Fig. 2d and Extended Data Fig. 4e–g). Together, these cryo-EM and NMR data define a Ctc1 binding motif (CBM) adjacent to the p50 OB domain that associates tightly with Ctc1 but allows a hinging movement of the entire TtCST complex on p50. Deletion of residues containing this motif results in loss of cell viability[43], indicating the importance of TtCST association with telomerase in vivo.

Overall structure of PolαPrim with CST

A defining feature of CST function at telomere ends is its ability to recruit PolαPrim for C-strand synthesis[10,26–29,44]. To both verify that Ctc1–Stn1–Ten1 is functionally TtCST and define the structural basis of PolαPrim recruitment, we assembled the *Tetrahymena* telomerase–PolαPrim complex using endogenously expressed telomerase and recombinant PolαPrim in the presence of sstDNA $d(GTTGGG)_{10}$, and determined its cryo-EM structure (Fig. 3a,b and Extended Data Figs. 5 and 6). We verified that this complex was active for both G-strand synthesis by

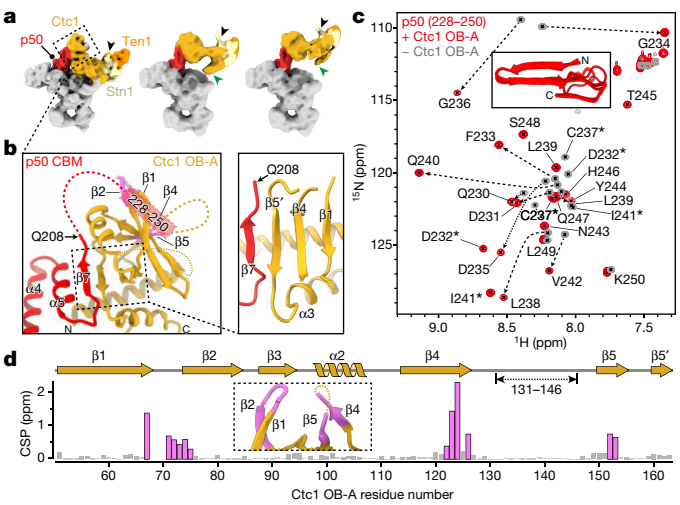

Fig. 2 | Interface between TtCST and p50. a, Cryo-EM maps of the telomerase holoenzyme with TtCST at different positions. TtCST subunits and p50 are coloured as indicated. The three-helix bundle and zinc ribbon motif are labelled with black and green arrows, respectively. Cryo-EM maps are low-pass filtered to similar resolution for comparison. **b**, Interactions between Ctc1 OB-A and p50 CBM. Unmodelled regions in the cryo-EM structure are shown as dashed lines. **c**, ^{1}H-^{15}N HSQC spectra of ^{15}N-labelled p50 peptide (residues 228–250) with (red) and without (grey) Ctc1 OB-A. NMR signals from the same residues are connected with dashed arrows or labelled with asterisks. Inset, the 10 lowest-energy CS-Rosetta models of p50 peptide (root mean squared deviation (r.m.s.d.) of Cα atoms = 1.73 Å) in the presence of Ctc1 OB-A. **d**, Chemical shift perturbation (CSP) index of ^{15}N-labelled Ctc1 OB-A upon binding to p50 peptide. Residues with CSP greater than 0.25 ppm are highlighted in magenta and their locations on the cryo-EM structure are shown in the inset and in **b**.

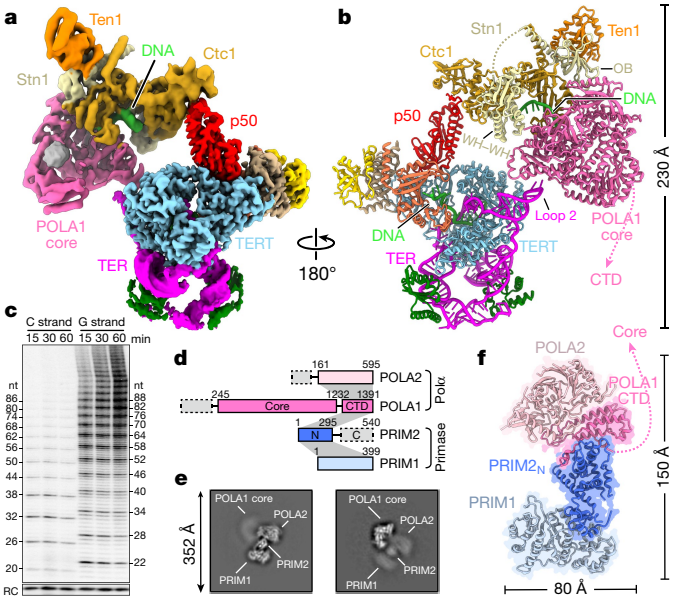

Fig. 3 | Structure of *Tetrahymena* telomerase holoenzyme in complex with PolαPrim. a, Composite map of the complex generated with focused refined cryo-EM maps (Extended Data Fig. 6a). **b**, Atomic model of the complex. The unstructured linker between the Stn1 OB and WH–WH domains is shown as a dashed line. **c**, Concurrent time courses of G-strand and C-strand synthesis by telomerase–PolαPrim using d(GTTGGG)$_3$ DNA primers (Methods). [^{32}P]dGTP and [^{32}P]dCTP were used to label the G-strand and C-strand products, respectively. The G-strand products provide the template for C-strand synthesis. RC, recovery control. Gel source data for all figures is provided in Supplementary Fig. 1. **d**, Structure-based schematic of PolαPrim. Intermolecular interactions between subunits are indicated as grey shading. **e**, Representative 2D class averages of PolαPrim. **f**, Cryo-EM structure of PolαPrim. The flexible linker between POLA1$_{core}$ and POLA1$_{CTD}$ is shown as a dashed line.

telomerase and C-strand synthesis by telomerase-associated CST–PolαPrim individually (Extended Data Fig. 5i) and for handoff of the G-strand on telomerase to PolαPrim for C-strand synthesis (Fig. 3c) using direct telomerase and PolαPrim activity assays. Using d(GTTGGG)$_{10}$ as template, as in the cryo-EM sample, TtCST–PolαPrim could copy the entire G-strand template (Extended Data Fig. 5i). By contrast, almost no C-strand synthesis was observed with PolαPrim alone (Extended Data Fig. 5i).

In the telomerase holoenzyme, PolαPrim binds TtCST in the absence or presence of sstDNA (Extended Data Fig. 5f). As the entire TtCST–PolαPrim complex was flexibly positioned relative to p50, as seen for TtCST alone, the TtCST–PolαPrim and telomerase-core RNP–TEB–p50 complexes were processed separately to obtain cryo-EM reconstructions of 4.2 Å and 2.9 Å resolution, respectively (Fig. 3a, Extended Data Fig. 6 and Extended Data Table 1). Together, we have a complete telomere DNA synthesis complex. Modelling of TtCST in the complex by initial rigid-body fitting of the structure determined in the absence of PolαPrim revealed the presence of additional density on Ctc1 OB-B and OB-C that could be fit with the crystal structure of Stn1 WH–WH[22,23] (Fig. 3b and Extended Data Fig. 6i). Binding of PolαPrim to TtCST displaces Ctc1 from its stable position across the top of the TERT ring (compare Fig. 3a,b with Fig. 1a,b), and instead POLA1 is positioned near TER loop 2. The Stn1 WH–WH binding site on Ctc1 would be occluded in the stable conformation of TtCST on p50–TERT in the absence of PolαPrim.

PolαPrim comprises two polymerase (POLA1 and POLA2) and two primase (PRIM1 and PRIM2) subunits[7,8] (Fig. 3d). The presence of all four subunits in the complex was confirmed by silver-stained SDS–PAGE (Extended Data Fig. 5f) and negative-stain electron microscopy 2D classification analysis (Extended Data Fig. 5g). However, only the catalytic POLA1 core domain (POLA1$_{core}$) was well resolved in the cryo-EM map (Fig. 3a,d). The rest of PolαPrim appears as a fuzzy density connected to POLA1$_{core}$ opposite the interface with Ctc1 (Extended Data Fig. 5g). Therefore, we also investigated the cryo-EM structure of PolαPrim alone, and obtained a 4.0–4.3 Å resolution structure for POLA2–POLA1$_{CTD}$–PRIM2$_N$–PRIM1 (where POLA1$_{CTD}$ is the POLA1 C-terminal domain and PRIM2$_N$ is the N-terminal domain of PRIM2) (Fig. 3e,f, Extended Data Fig. 7 and Extended Data Table 1). Two-dimensional class averages of PolαPrim show that POLA2–POLA1$_{CTD}$–PRIM2$_N$–PRIM1 forms a platform that holds POLA1$_{core}$ in various positions (Fig. 3e). We generated initial models of PolαPrim subunits with AlphaFold2, rigid-body fit them into corresponding densities and adjusted them manually (Methods). The structures of the individual subunits are highly similar to those of human PolαPrim[45–47] (Extended Data Fig. 8a,b). However, POLA2–POLA1$_{CTD}$ and PRIM1—which are located on either end of the platform—appear to be able to rotate relative to each other, with PRIM2$_N$ as the pivot (Extended Data Fig. 8b). The C-terminal domain of PRIM2 (PRIM2$_C$)—which specifically interacts with and coordinates RNA–DNA duplex translocation from the active site on PRIM1 to the active site on POLA1$_{core}$[8]—was not observed during cryo-EM data processing, suggesting that its position is dynamic. This flexible organization of PolαPrim would allow the large-scale domain movements that are expected for the switch from RNA primer to C-strand DNA synthesis[8]. Previous structures of human PolαPrim determined by X-ray crystallography and cryo-EM of a crosslinked sample are in an autoinhibited conformation (Extended Data Fig. 8c), with the active site on POLA1$_{core}$ sterically blocked for DNA entry by POLA1$_{CTD}$ and POLA2[45,46]. Our studies provide structures of a PolαPrim compatible with activity and establish its direct interactions with TtCST.

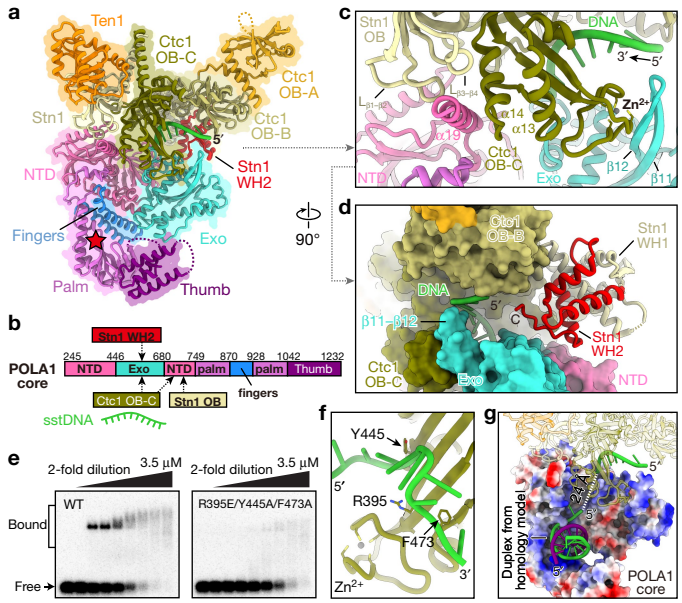

Fig. 4 | Interface between TtCST and POLA1$_{core}$. **a**, Ribbon representation of TtCST and POLA1$_{core}$ with individual proteins, domains and motifs coloured as indicated. The location of the POLA1 active site is shown as a red star. **b**, Structure-based schematic of POLA1$_{core}$ and interactions with TtCST. **c**,**d**, Close-up views of the interface between POLA1$_{core}$ and TtCST with sstDNA shown from perpendicular directions. **e**, EMSA of d(GTTGGG)$_5$ DNA binding by wild-type (WT) and Ctc1 mutant TtCST. Wedges indicate a series of twofold dilutions of TtCST from 3.5 to 0.03 μM. The first lane of each gel is a CST-free control. Quantification of EMSAs is shown in Extended Data Fig. 9j. **f**, The sstDNA binding site on Ctc1 OB-C. Side chains of residues substituted for EMSA are shown as sticks. **g**, Close-up view of POLA1$_{core}$ (electrostatic surface) with a DNA duplex modelled on the basis of the human POLA1 structure[47] (Protein Data Bank (PDB) 5IUD). The template and product strands in the duplex are coloured in green (G-strand) and purple (C-strand), respectively. The path of sstDNA in the channel is shown as a dashed line.

CST interaction with POLA1 and sstDNA

POLA1$_{core}$ comprises an N-terminal domain (NTD) that brackets a catalytically dead exonuclease (Exo), and a C-terminal DNA polymerase that contains palm, finger and thumb domains[8] (Fig. 4a,b). All elements of POLA1$_{core}$ except the tip of the thumb are well defined in the cryo-EM map. TtCST interacts with POLA1$_{core}$ via Ctc1 OB-C and Stn1, and the interface has a surface area of around 1,120 Å^2 (Fig. 4a–d and Extended Data Fig. 9). On Ctc1 OB-C, the conserved zinc ribbon motif interacts primarily with the conserved Exo β11–β12 hairpin (Fig. 4c and Extended Data Fig. 8d). The Ctc1 helix α14 and Stn1 OB β1–β2 and β3–β4 loops form a binding pocket that accommodates POLA1$_{core}$ NTD helix α19 (residues 731–748) with charge complementarity to its side chains (Fig. 4c and Extended Data Fig. 8e–g). Helix α19 is a flexible loop in all other structures of PolαPrim[45–47], and appears to become structured only on binding Ctc1–Stn1 (Extended Data Fig. 8e), indicating the importance of this interaction for TtCST binding. Behind this interface, the three helices of the Stn1 winged helix 2 (WH2) domain are inserted into a gap between Ctc1 OB-B and POLA1 Exo (Fig. 4d). The structure shows that POLA1$_{core}$ Exo and NTD form an extensive interface with TtCST involving Ctc1 OB-C, the Stn1 OB domain and Stn1 WH–WH, which is otherwise flexibly tethered to the Stn1 OB domain in the absence of PolαPrim. Structure-based sequence alignment suggests conservation of these regions in POLA1$_{core}$ that interface with TtCST across a wide range of species (Extended Data Fig. 8g).

Cryo-EM density for approximately ten nucleotides of sstDNA is observed on Ctc1 OB-C across the C-shaped binding cleft near the zinc ribbon (Fig. 4a,c), but side-chain interactions cannot be discerned. Substitution of three residues (R395E/Y445A/F473A) on the apparent binding surface increases the equilibrium dissociation constant (K_D) for sstDNA binding to purified TtCST by approximately threefold (from 0.18 to 0.52 μM), as determined by electromobility shift assays (EMSA) with d(GTTGGG)$_5$ (Fig. 4e,f and Extended Data Fig. 9f–k), verifying the observed DNA-binding site. The sstDNA extends 5′ to 3′ into an entry port formed by POLA1$_{core}$ NTD and Exo and Ctc1 OB-C (Extended Data Fig. 8h) of a highly basic channel that leads to the active site of POLA1 approximately 40 Å away, where the primer–sstDNA duplex would bind (Fig. 4g). Since sstDNA is added in excess during the purification, both telomerase and TtCST can bind separate sstDNA strands. No density for sstDNA is visible on TtCST in the absence of PolαPrim, perhaps owing to dynamics and/or steric occlusion by interaction of Ctc1 with TERT in the predominant conformation (Fig. 1b and Extended Data Fig. 2i–l).

The sstDNA on Ctc1 OB-C appears positioned for entry into a template (G-strand) binding tunnel on POLA1$_{core}$, and there is weak density in the tunnel that we attribute to sstDNA (Extended Data Fig. 8i,j), suggesting the possibility that this structure has captured the polymerase mode after handoff from primase. Although no DNA–RNA or DNA–DNA duplex is present in the active site of POLA1, there is unassigned density between POLA1$_{core}$ palm and thumb (Fig. 3a) that fits the dimensions of a G-quadruplex formed by four *Tetrahymena* telomere DNA repeats[48] (Extended Data Fig. 8j). *Tetrahymena* telomere DNA repeats can form unimolecular G-quadruplexes with three or four G-quartets in the presence of Na^+ or K^+, respectively[48,49], whereas G-quadruplexes do not form with Li^+ in the absence of other cations. Addition of 50 mM of these cations individually to the activity assay buffer for telomerase–PolαPrim with d(GTTGGG)$_{10}$ prepared as for the cryo-EM studies decreases C-strand synthesis in the order of increasing G-quadruplex stability[50]—that is, $Li^+ > Na^+ > K^+$ (Extended Data Fig. 5j). Given that the newly synthesized telomeric DNA is single-stranded as it exits onto Teb1[40], the slow folding kinetics of G-quadruplexes probably limit the amount of G-quadruplex formed *in vivo* before G-strand binding on CST–PolαPrim. We propose that the apparent G-quadruplex present in the cryo-EM density may have serendipitously trapped PolαPrim in an incipient inhibited DNA polymerization state. Overall, the structure defines the interface between POLA1 and CST and the pathway of the G-strand from CST to the active site of POLA1, where it provides the template for C-strand synthesis.

Comparison with human CST

Tetrahymena Stn1 and Ten1 have the same domain structure as human STN1 and TEN1, respectively; however, human CTC1 is much larger than *Tetrahymena* Ctc1, with seven OB domains[19] (OB-A to OB-G) (Fig. 5a,b and Extended Data Fig. 9a) that may have arisen from a gene duplication of RPA70. A DALI search of Ctc1 against all proteins in the Protein Data Bank (Methods) found the highest structural similarity with human CTC1 (*Z*-score 14.5). For the individual domains, Ctc1 OB-B and OB-C are most similar to human CTC1 OB-F and OB-G, respectively (Extended Data Fig. 9b,c). A cryo-EM study of human CST with bound sstDNA revealed a decameric structure with D_5 symmetry[19]. Comparing the human CST monomer extracted from the decamer with TtCST shows that Ten1 and TEN1, the Stn1 OB and STN1 OB domains, and Ctc1 OB-A–C and CTC1 OB-E–G are positioned similarly (Fig. 5a,b). However, Stn1 WH–WH, which is visible only in the PolαPrim-bound TtCST structure, is positioned on Ctc1 OB-B and OB-C (Fig. 5a and Extended Data Fig. 9d), whereas in human CST, STN1 WH–WH is positioned on CTC1 OB-E and sticks out from the decamer in the 'arm' conformation[19] (Fig. 5b,c). Of note, low-resolution cryo-EM densities of monomeric human CST revealed an additional 'head' conformation[19], in which the human STN1 WH–WH occupies a position apparently similar to that observed

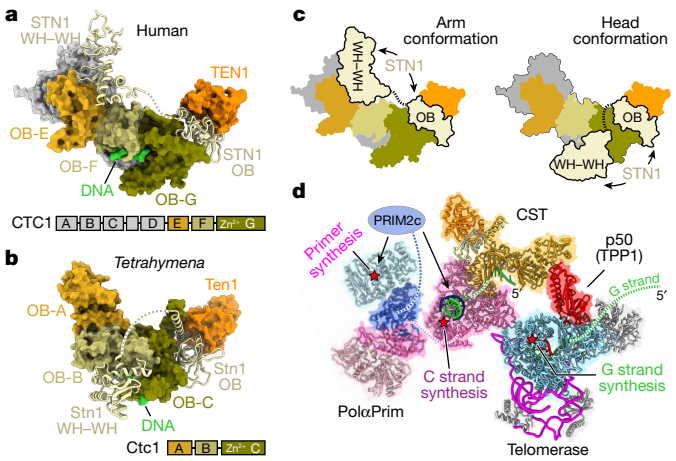

Fig. 5 | Structural comparison of *Tetrahymena* and human CST. a,**b**, Surface representation of human CST[19] (PDB 6W6W) (**a**) and TtCST (**b**) with Stn1 and STN1 shown as ribbons. Corresponding subunits and domains are coloured the same, as indicated. **c**, Cartoons of human CST with STN1 WH–WH in arm and head conformations[19]. The linker between the STN1 OB domain and WH–WH is shown as a dashed line. **d**, Model of *Tetrahymena* telomerase holoenzyme in complex with PolαPrim. The DNA duplex on $POLA1_{core}$ is modelled on the basis of a homology model[47] of human $POLA1_{core}$ (PDB 5IUD). The position of the $POLA2–POLA1_{CTD}–PRIM2_N–PRIM1$ platform relative to $POLA1_{core}$ is based on a low-resolution cryo-EM map in Extended Data Fig. 7a. Telomeric DNA G-strand and C-strand are coloured green and purple, respectively. $PRIM2_C$ is shown as an oval connecting to $PRIM2_N$. Active sites on TERT, PRIM1 and POLA1 for the synthesis of G-strand, C-strand primer and C-strand, respectively, are denoted by red stars. During G-strand and C-strand synthesis, these active sites would be occupied successively for a given G-strand, and not simultaneously.

in TtCST-bound PolαPrim (Fig. 5c). In our structure, Stn1 WH–WH in this position forms part of the interface with PolαPrim (Fig. 4d). If human CST binds PolαPrim in a similar manner to TtCST, it could only bind as a monomer, since the binding interface would be occluded by intermonomer interactions in the human CST decamer.

Different but adjacent binding sites for sstDNA are observed for equivalent regions on the human CST decamer[19] versus TtCST (Fig. 5a,b and Extended Data Fig. 9e). For human CST, the four DNA nucleotides visible in the decameric structure interact with human CTC1 OB-F (Extended Data Fig. 9e), and two of them also interact with OB-G[19]. Comparison of Ctc1 OB-B with CTC1 OB-F shows sequence similarity for the residues on the OB-F binding cleft that interact with the four DNA nucleotides (Extended Data Fig. 9f). To investigate whether there might be a similar DNA interaction on *Tetrahymena* Ctc1 OB-B (in addition to the ten nucleotides that we observe on OB-C), we substituted three conserved residues (K303E/K306E/F308A), equivalent to a set shown to increase K_D of human CST for sstDNA[13,19]. These substitutions increase the K_D for $d(GTTGGG)_5$ by approximately 1.5-fold as assayed by EMSA (Extended Data Fig. 9i–k). Substitution of two conserved aromatic residues (F264A/Y268A) that may contribute to DNA binding through stacking interactions[13,19] increases K_D by 1.2-fold (Extended Data Fig. 9i–k). Together, these comparisons suggest that human CTC1 C-terminal OB-E, OB-F and OB-G may interact with POLA1 and sstDNA in a similar manner to Ctc1 OB-A, OB-B and OB-C, and that the PolαPrim interaction may only be accommodated in monomeric CST.

Coordinated synthesis of G- and C-strands

Coordinated synthesis of telomeric G- and C-strands in vertebrates is orchestrated by interactions between telomerase, the shelterin proteins TPP1 and POT1, sstDNA, CST and PolαPrim, whose molecular details have remained largely undefined. Here, taking advantage of the constitutive association of p50 (a TPP1 orthologue), Teb1 (a POT1 orthologue) and TtCST with *Tetrahymena* telomerase, along with previous structural studies of telomerase[22,40], we determined the structures and interfaces between all of these components. *Tetrahymena* Ctc1 C-terminal domain OB-C and Stn1 bind to PolαPrim POLA1 and Ctc1 N-terminal domain OB-A binds p50 (Fig. 5d). The p50 OB domain in turn binds to TERT TEN–TRAP domains—constitutively in *Tetrahymena* but transiently to recruit telomerase to telomeres in humans[32,33,40]. Biochemical studies have shown that human CST binds G-strands released from telomerase during telomere-repeat synthesis[12,13], and our structures and activity assays verify these results in *Tetrahymena*. Our structures show that TtCST binds p50 on a flexible hinge (CBM), placing it in the proximity of where the 3′ end of sstDNA released from the TER template would be. Teb1, which also interacts with p50 and the TERT TEN domain, may contribute by initially maintaining a hold on the 5′ exiting DNA until it binds CST. C-strand synthesis requires that the G-strand is released from telomerase catalytic core to provide the 3′ end of the G-strand as the template for C-strand synthesis. PRIM2c has been proposed to bind the RNA–DNA duplex and hand it off from the primase to the active site of POLA1[8] (Fig. 5d). Our structure explains how CST enhances the activity of POLA1, by binding the G-strand and feeding it into the entry port for the POLA1 template channel (Fig. 4g). The autoinhibited conformation of PolαPrim[45,46] would be occluded in the CST–PolαPrim complex, possibly explaining how CST could enhance the primase-to-polymerase switch[44]. It is less clear how CST binding could activate PRIM1 for primer synthesis, consistent with proposals for a large conformational switch between priming and polymerization steps[8]. Here we have captured a pre-DNA C-strand polymerization step in a PolαPrim complex with the *Tetrahymena* telomerase-core RNP, CST, p50 and TEB, linking G-strand and C-strand synthesis in an almost complete telomere end replicon.

Online content

Any methods, additional references, Nature Research reporting summaries, source data, extended data, supplementary information, acknowledgements, peer review information; details of author contributions and competing interests; and statements of data and code availability are available at https://doi.org/10.1038/s41586-022-04931-7.

1. de Lange, T. Shelterin-mediated telomere protection. *Annu. Rev. Genet.* **52**, 223–247 (2018).
2. Lim, C. J. & Cech, T. R. Shaping human telomeres: from shelterin and CST complexes to telomeric chromatin organization. *Nat. Rev. Mol. Cell Biol.* **22**, 283–298 (2021).
3. Baumann, P. & Cech, T. R. Pot1, the putative telomere end-binding protein in fission yeast and humans. *Science* **292**, 1171–1175 (2001).
4. Abreu, E. et al. TIN2-tethered TPP1 recruits human telomerase to telomeres in vivo. *Mol. Cell. Biol.* **30**, 2971–2982 (2010).
5. Nandakumar, J. et al. The TEL patch of telomere protein TPP1 mediates telomerase recruitment and processivity. *Nature* **492**, 285–289 (2012).
6. Greider, C. W. & Blackburn, E. H. Identification of a specific telomere terminal transferase activity in *Tetrahymena* extracts. *Cell* **43**, 405–413 (1985).
7. Pellegrini, L. The Pol α-primase complex. *Subcell. Biochem.* **62**, 157–169 (2012).
8. Baranovskiy, A. G. & Tahirov, T. H. Elaborated action of the human primosome. *Genes* **8**, 62 (2017).
9. Qi, H. & Zakian, V. A. The *Saccharomyces* telomere-binding protein Cdc13p interacts with both the catalytic subunit of DNA polymerase α and the telomerase-associated Est1 protein. *Genes Dev.* **14**, 1777–1788 (2000).
10. Wang, F. et al. Human CST has independent functions during telomere duplex replication and C-strand fill-in. *Cell Rep.* **2**, 1096–1103 (2012).
11. Surovtseva, Y. V. et al. Conserved telomere maintenance component 1 interacts with STN1 and maintains chromosome ends in higher eukaryotes. *Mol. Cell* **36**, 207–218 (2009).
12. Chen, L. Y., Redon, S. & Lingner, J. The human CST complex is a terminator of telomerase activity. *Nature* **488**, 540–544 (2012).
13. Zaug, A. J. et al. CST does not evict elongating telomerase but prevents initiation by ssDNA binding. *Nucleic Acids Res.* **49**, 11653–11665 (2021).
14. Stewart, J. A. et al. Human CST promotes telomere duplex replication and general replication restart after fork stalling. *EMBO J.* **31**, 3537–3549 (2012).
15. Mirman, Z. et al. 53BP1–RIF1–shieldin counteracts DSB resection through CST- and Polα-dependent fill-in. *Nature* **560**, 112–116 (2018).
16. Holohan, B., Wright, W. E. & Shay, J. W. Telomeropathies: an emerging spectrum disorder. *J. Cell Biol.* **205**, 289–299 (2014).

17. Chen, L. Y., Majerska, J. & Lingner, J. Molecular basis of telomere syndrome caused by CTC1 mutations. *Genes Dev.* **27**, 2099–2108 (2013).
18. Prakash, A. & Borgstahl, G. E. The structure and function of replication protein A in DNA replication. *Subcell. Biochem.* **62**, 171–196 (2012).
19. Lim, C. J. et al. The structure of human CST reveals a decameric assembly bound to telomeric DNA. *Science* **368**, 1081–1085 (2020).
20. Ge, Y. et al. Structural insights into telomere protection and homeostasis regulation by yeast CST complex. *Nat. Struct. Mol. Biol.* **27**, 752–762 (2020).
21. Bryan, C., Rice, C., Harkisheimer, M., Schultz, D. C. & Skordalakes, E. Structure of the human telomeric Stn1–Ten1 capping complex. *PLoS ONE* **8**, e66756 (2013).
22. Jiang, J. et al. Structure of *Tetrahymena* telomerase reveals previously unknown subunits, functions, and interactions. *Science* **350**, aab4070 (2015).
23. Wan, B. et al. The *Tetrahymena* telomerase p75–p45–p19 subcomplex is a unique CST complex. *Nat. Struct. Mol. Biol.* **22**, 1023–1026 (2015).
24. Kratz, K. & de Lange, T. Protection of telomeres 1 proteins POT1a and POT1b can repress ATR signaling by RPA exclusion, but binding to CST limits ATR repression by POT1b. *J. Biol. Chem.* **293**, 14384–14392 (2018).
25. Wan, M., Qin, J., Songyang, Z. & Liu, D. OB fold-containing protein 1 (OBFC1), a human homolog of yeast Stn1, associates with TPP1 and is implicated in telomere length regulation. *J. Biol. Chem.* **284**, 26725–26731 (2009).
26. Kelich, J. M., Papaioannou, H. & Skordalakes, E. Pol α-primase dependent nuclear localization of the mammalian CST complex. *Commun. Biol.* **4**, 349 (2021).
27. Ganduri, S. & Lue, N. F. STN1–POLA2 interaction provides a basis for primase-pol α stimulation by human STN1. *Nucleic Acids Res.* **45**, 9455–9466 (2017).
28. Feng, X., Hsu, S. J., Kasbek, C., Chaiken, M. & Price, C. M. CTC1-mediated C-strand fill-in is an essential step in telomere length maintenance. *Nucleic Acids Res.* **45**, 4281–4293 (2017).
29. Feng, X. et al. CTC1–STN1 terminates telomerase while STN1–TEN1 enables C-strand synthesis during telomere replication in colon cancer cells. *Nat. Commun.* **9**, 2827 (2018).
30. Wang, Y., Susac, L. & Feigon, J. Structural biology of telomerase. *Cold Spring Harb. Perspect. Biol.* **11**, a032383 (2019).
31. Wang, F. et al. The POT1–TPP1 telomere complex is a telomerase processivity factor. *Nature* **445**, 506–510 (2007).
32. Sekne, Z., Ghanim, G. E., van Roon, A. M. & Nguyen, T. H. D. Structural basis of human telomerase recruitment by TPP1–POT1. *Science* **375**, 1173–1176 (2022).
33. Liu, B. et al. Structure of active human telomerase with telomere shelterin protein TPP1. *Nature* **604**, 578–583 (2022).
34. Upton, H. E., Chan, H., Feigon, J. & Collins, K. Shared subunits of *Tetrahymena* telomerase holoenzyme and replication protein A have different functions in different cellular complexes. *J. Biol. Chem.* **292**, 217–228 (2017).
35. Zeng, Z. et al. Structural basis for *Tetrahymena* telomerase processivity factor Teb1 binding to single-stranded telomeric-repeat DNA. *Proc. Natl Acad. Sci. USA* **108**, 20357–20361 (2011).
36. Lei, M., Podell, E. R. & Cech, T. R. Structure of human POT1 bound to telomeric single-stranded DNA provides a model for chromosome end-protection. *Nat. Struct. Mol. Biol.* **11**, 1223–1229 (2004).
37. Chen, C. et al. Structural insights into POT1–TPP1 interaction and POT1 C-terminal mutations in human cancer. *Nat. Commun.* **8**, 14929 (2017).
38. Rice, C. et al. Structural and functional analysis of the human POT1–TPP1 telomeric complex. *Nat. Commun.* **8**, 14928 (2017).
39. Jiang, J. et al. Structure of telomerase with telomeric DNA. *Cell* **173**, 1179–1190.e1113 (2018).
40. He, Y. et al. Structures of telomerase at several steps of telomere repeat synthesis. *Nature* **593**, 454–459 (2021).
41. Ghanim, G. E. et al. Structure of human telomerase holoenzyme with bound telomeric DNA. *Nature* **593**, 449–453 (2021).
42. Wang, Y., Gallagher-Jones, M., Sušac, L., Song, H. & Feigon, J. A structurally conserved human and *Tetrahymena* telomerase catalytic core. *Proc. Natl Acad. Sci. USA* **117**, 31078–31087 (2020).
43. Hong, K. et al. *Tetrahymena* telomerase holoenzyme assembly, activation, and inhibition by domains of the p50 central hub. *Mol. Cell. Biol.* **33**, 3962–3971 (2013).
44. Lue, N. F., Chan, J., Wright, W. E. & Hurwitz, J. The CDC13–STN1–TEN1 complex stimulates Pol α activity by promoting RNA priming and primase-to-polymerase switch. *Nat. Commun.* **5**, 5762 (2014).
45. Baranovskiy, A. G. et al. Mechanism of concerted RNA–DNA primer synthesis by the human primosome. *J. Biol. Chem.* **291**, 10006–10020 (2016).
46. Kilkenny, M. L. et al. Structural basis for the interaction of SARS-CoV-2 virulence factor nsp1 with DNA polymerase α-primase. *Protein Sci.* **31**, 333–344 (2022).
47. Coloma, J., Johnson, R. E., Prakash, L., Prakash, S. & Aggarwal, A. K. Human DNA polymerase α in binary complex with a DNA:DNA template–primer. *Sci Rep.* **6**, 23784 (2016).
48. Beseiso, D. et al. The first crystal structures of hybrid and parallel four-tetrad intramolecular G-quadruplexes. *Nucleic Acids Res.* **50**, 2959–2972 (2022).
49. Bryan, T. M. G-quadruplexes at telomeres: friend or foe? *Molecules* **25**, 3686 (2020).
50. Williamson, J. R., Raghuraman, M. K. & Cech, T. R. Monovalent cation-induced structure of telomeric DNA: the G-quartet model. *Cell* **59**, 871–880 (1989).

Methods

Tetrahymena PolαPrim cloning and expression

Tetrahymena PolαPrim complexes were expressed using the Bac-to-Bac system (Thermo Fisher Scientific) in Sf9 cells. In brief, cDNAs encoding *Tetrahymena* POLA1 (UniProt accession number: Q23AJ0), POLA2 (I7MAE1), PRIM1 (Q24HY6) and PRIM2 (Q246C7) were chemically synthesized and purchased from IDT (Integrated DNA Technologies). To co-express the POLA1–POLA2 complex, POLA1 and POLA2 cDNAs were cloned into a pFastBacDual vector (Thermo Fisher Scientific), under the polyhedrin promoter and the p10 promoter, respectively. The POLA1 has an N-terminal hexahistidine tag and tobacco etch virus protease cleavage site (His_6–TEV). To co-express the POLA1–POLA2–PRIM1–PRIM2 complex, PRIM1 and PRIM2 cDNAs were cloned into a separate pFastBacDual vector. The expression vectors were used to make baculoviruses based on the established protocol for Bac-to-Bac system (Thermo Fisher Scientific). *Sf9* cells (2.0×10^6 ml^{-1}) were transfected with viruses using a multiplicity of infection (MOI) of 3 at 27 °C in SF-900 II SFM medium (Thermo Fisher Scientific). The cells were collected 48 h after infection and stored at −80 °C until purification.

TtCST–p50 cloning and expression

TtCST–p50 complex was expressed in insect cells. In brief, cDNAs encoding p50 (D2CVN8), p75 (A0PGB2), p45 (Q6JXI5) and p19 (D2CVN7) were chemically synthesized and purchased from IDT (Integrated DNA Technologies). The Ctc1 and p50 cDNAs were cloned into a pFastBacDual vector (Thermo Fisher Scientific), with a His_6-TEV tag fused onto the N-terminal of Ctc1. The Stn1 and Ten1 cDNAs were cloned into a separate pFastBacDual vector for baculoviruses expression. Sf9 cells (2.1×10^6 ml^{-1}) were transfected with viruses using a MOI of 3 at 27 °C in SF-900 II SFM medium (Thermo Fisher Scientific). The cells were collected 48 h after infection and stored at −80 °C until purification.

Purification of *Tetrahymena* PolαPrim and CST–p50 complexes

The purification steps for both POLA1–POLA2–PRIM1–PRIM2 and p50–Ctc1–Stn1–Ten1 were performed at 4 °C using an AKTA chromatography system with prepacked columns (GE Healthcare) following the same protocol. Cells were suspended in buffer A (30 mM Tris-HCl (pH 7.5), 200 mM NaCl, 10% (v/v) glycerol, 1 mM dithiothreitol (DTT) and 25 mM imidazole) supplemented with protease inhibitor cocktail (Sigma), lysed by sonication, and centrifuged at 34,000*g* for 1 h. The supernatant was applied onto a 5-ml HisTrap HP column pre-equilibrated in buffer A. The column was washed with buffer A and the complex was eluted with buffer B (30 mM Tris-HCl (pH 7.5), 1 M NaCl, 10% (v/v) glycerol, 1 mM DTT and 400 mM imidazole). The protein complex was digested overnight with 0.2 mg ml^{-1} TEV protease and buffer exchanged to buffer A. The digest was applied onto a 5-ml HisTrap HP column pre-equilibrated in buffer A. The target complex was isolated in the column flow-through, concentrated to 10 ml, and then applied onto a Superdex 200 gel filtration column pre-equilibrated in buffer C (25 mM Tris-HCl (pH 7.5), 150 mM NaCl and 1 mM DTT). The complex was collected from peak fractions and analysed by SDS polyacrylamide gel electrophoresis.

NMR sample preparation

cDNAs of Ctc1 OB-A (residues 1–183) and p50 peptides (Extended Data Fig. 4a) were cloned into the pETduet vector with a His_6-MBP-TEV tag at the N terminus of each construct, and expressed by *Escherichia coli* strain BL21(DE3). ^{2}H,^{13}C and ^{15}N-labelled Ctc1 OB-A was expressed from M9 minimal medium supplemented with 0.5 l D_2O, 2 g [^{13}C]D-glucose and 0.5 g of [^{15}N]ammonium chloride, and ^{13}C and ^{15}N-labelled p50 peptide was expressed from M9 minimal medium supplemented with [^{13}C]D-glucose and of [^{15}N]ammonium chloride. Cultures were grown to mid-log phase at 37 °C, induced by the addition of β-D-1-thiogalactopyranoside to a final concentration of 0.5 mM, and incubated at 18 °C for an additional 12 h before collection by centrifugation. The purification steps for Ctc1 OB-A and p50 peptides were similar to those for *Tetrahymena* PolαPrim described above. In brief, cells were re-suspended in buffer A, lysed by sonication and centrifuged at 4,500*g* for 30 min. The supernatant was loaded onto a 5-ml HisTrap HP column pre-equilibrated in buffer A. The column was washed with buffer A and the protein was eluted with buffer B. The protein was digested overnight with 0.2 mg ml^{-1} TEV protease and buffer exchanged to buffer A. The digest was applied onto a 5-ml HisTrap HP column pre-equilibrated in buffer A. The flow-through was concentrated and further purified on an Superdex 75 gel filtration column pre-equilibrated in buffer C. Fractions containing pure protein were pooled, buffer exchanged into protein NMR buffer (20 mM Tris (pH 7.5), 50 mM NaCl, 1 mM Tris(2-carboxyethyl)phosphine (TCEP), 3 mM NaN_3 and 8% D_2O), and concentrated to 0.5–0.8 mM for NMR studies.

NMR spectroscopy and data processing

NMR experiments were performed at 298 K on 800 and 600 MHz Bruker spectrometers equipped with HCN cryoprobes. The backbone assignments of Ctc1 OB-A were obtained using the TROSY-type HNCACB, HN(CO)CACB, HNCA, HN(CO)CA, HNCO, and HN(CA)CO spectra collected on an 800 MHz Bruker instrument with ^{2}H,^{13}C,^{15}N-labelled Ctc1 OB-A. Conventional triple resonance backbone assignment experiments (HNCACB, CBCA(CO)NH, HNCA, HN(CO)CA) were used for p50 peptide (228–250) backbone assignments. Spectra were collected and processed using Topspin 4.1, and analysed with CARA (http://cara.nmr.ch) and NMRFAM Sparky[51] to interactively obtain sequence-specific resonance assignments. NOE peak lists were automatically generated by Atnos[52], and assigned by CYANA 3.98[53]. Secondary structure of Ctc1 OB-A and p50 peptide (228–250) were predicted by TALOS+[54]. Models of p50 peptide (228–250) were predicted by CS-Rosetta[55] using chemical shift data. Cα r.m.s.d. of the 10 lowest-energy models is 1.73 Å, suggesting a high confidence of the prediction. To investigate the interaction between Ctc1 OB-A and p50 peptides, ^{1}H-^{15}N HSQC spectra of titration of unlabelled p50 peptides with labelled Ctc1 OB-A and titration of unlabelled Ctc1 OB-A with labelled p50 peptides were obtained. Chemical shift mapping was analysed by comparing the apo and bound-form HSQC spectra. The CSP value for each residue was calculated as $CSP = \sqrt{((\triangle \delta HN)^2 + 0.14 \times (\triangle \delta N)^2)/2}$, where the $\triangle$δHN and $\triangle$δN are the change ($\triangle$) in chemical shift (δ) of HN and N resonances from apo to bound (ref. [56]). The backbone assignments of ^{2}H,^{13}C and ^{15}N-labelled Ctc1 OB-A in the presence of unlabelled p50 peptide (228–250) were obtained using the same TROSY-type spectra as listed above, while the backbone assignment of ^{13}C and ^{15}N-labelled p50 peptide (228–250) in the presence of unlabelled Ctc1 OB-A were obtained using conventional triple resonance spectra.

Telomerase sample preparation

Tetrahymena telomerase holoenzyme was expressed and purified as described previously[40,57]. To prepare the telomerase–PolαPrim complex sample, 0.5 μM of purified POLA1–POLA2–PRIM1–PRIM2 was incubated with telomerase holoenzyme at the anti-Flag M2 affinity gel (Sigma) step overnight at 4 °C, in the presence of excess $d(GTTGGG)_{10}$ primer. Excess DNA and PolαPrim were removed with wash buffer (20 mM HEPES (pH 8.0), 50 mM NaCl, 1 mM $MgCl_2$, 1 mM TCEP, 10% (v/v) glycerol, 0.1% (v/v) IGEPAL CA-630) and the final product was eluted using a small volume (30–50 μl) of elution buffer (20 mM HEPES (pH 8.0), 50 mM NaCl, 1 mM $MgCl_2$, 1 mM TCEP, and 0.1% (v/v) IGEPAL CA-630) supplemented with 1 mg ml^{-1} 3× Flag peptide.

Cryo-EM specimen preparation and data collection

For telomerase–PolαPrim complex, 3 μl of the purified sample was applied to glow-discharged lacey carbon grids with a supporting ultrathin carbon film (Ted Pella). The grids were then blotted with filter paper and flash-frozen in liquid ethane using an FEI Vitrobot Mark IV at 10 °C and 100% humidity. Cryo-EM grids of PolαPrim were

prepared similarly with Quantifoil 200 mesh R2/1 grids. Cryo-EM grids were loaded into a Thermo Fisher Titan Krios electron microscope operated at 300 kV for automated data collection using SerialEM[58]. Movies of dose-fractionated frames were acquired with a Gatan K3 direct electron detector in super-resolution mode at a pixel size of 0.55 Å on the sample level. A Gatan imaging filter was inserted between the electron microscope and the K3 camera and operated at zero-loss mode with the slit width of 20 eV. The microscope was carefully aligned prior to each imaging session and parallel beam was optimized using coma-free alignment in SerialEM. The total dose rate on the sample was set to ~55 electrons per $Å^2$, which was fractionated into 50 frames with 0.06 s exposure time for each frame. For telomerase–PolαPrim, 36,716 movies were collected in two separate imaging sessions with the same batch of cryo-EM grids. For PolαPrim, 7,120 movies were collected in a single imaging session.

Cryo-EM data processing

Cryo-EM data processing workflows are outlined in Extended Data Figs. 1, 6 and 7 for the structure determination of *Tetrahymena* (*Tt*) CST in telomerase, PolαPrim-bound TtCST in telomerase, and PolαPrim alone, respectively. All steps described below were performed with RELION 3.1[59] unless otherwise indicated.

To determine TtCST structure, telomerase particles selected from three published datasets (the T3D2, T4D4 and T5D5 datasets as detailed in ref. [40]) were combined, resulting in over 2.5 million good particles (Extended Data Fig. 1a). Refinement of these particles without a mask generated a reconstruction with only weak density for TtCST, which confirms the multiple orientation of TtCST relative to the rest of telomerase holoenzyme[22]. To separate particles with TtCST at different positions, an alignment-free 3D classification was performed using a spherical mask covering the TtCST region (mask1). Particles from classes with TtCST at similar positions were grouped together and refined, resulting in three reconstructions (P1, P2 and P3 in Extended Data Fig. 1a), among which P1 has the best density and the largest number of particles. To improve the overall density of P1, we performed another round of 3D classification with local angular search (RELION options: --sigma_ang 8 --healpix_order 4). A soft mask (mask2) was used in this step to exclude the flexible p65. 259,330 particles from the best class were selected for 3D refinement, following by refinement of contrast transfer function (CTF) parameters and Bayesian polishing in RELION. The resulting 'shiny' particles were refined to 3.5 Å resolution for the entire telomerase holoenzyme including TtCST (Extended Data Fig. 1b–d). An additional focused 3D classification step was conducted to improve the local resolution of Ctc1 OB-A. The resulting 78,471 particles were refined to 3.8 Å resolution using mask2.

For the newly collected telomerase–PolαPrim and PolαPrim datasets, dose-fractionated frames of each movie were 2× binned (pixel size of 1.1 Å), aligned for the correction of beam-induced drift, and dose weighted using RELION's implementation of UCSF MotionCor2[60]. CTF parameters, including defocus and astigmatism, of each dose-weighted micrograph were determined by CTFFIND4[61] within RELION.

Two datasets of telomerase–PolαPrim, one for each data collection session, were initially processed separately (Extended Data Fig. 6a). Particles picked from 2,000 representative micrographs using template-free auto-picking in RELION were screened by 2D classification, and the best particles were selected to train a particle detection model in Topaz[62] for subsequent neural-network based particle picking for all micrographs. After several rounds of 2D and 3D classifications as detailed in Extended Data Fig. 6a, good particles selected from two datasets were combined, resulting in over 1.6 million particles. Refinement of these particles without using any mask generated a reconstruction with only weak density for TtCST–PolαPrim, suggesting that TtCST–PolαPrim also has multiple orientations relative to the rest of telomerase holoenzyme, including telomerase core RNP, TEB heterotrimer and p50, as previously observed for the TtCST dataset (Extended Data Fig. 1a). Therefore, these two parts were processed separately in the following steps. For telomerase core RNP–TEB–p50, a soft mask was used to exclude the dynamic TtCST–PolαPrim during 3D refinement, which resulted in a 3.1 Å resolution reconstruction. After an additional round of focused classification with local angular search in 8° (RELION options: --sigma_ang 8 --healpix_order 4), 539,078 particles from the best class were selected and refined to 2.9 Å resolution (Extended Data Fig. 6b,c). For TtCST–PolαPrim, three rounds of alignment-free 3D classification with an optimized regularization parameter (RELION option: --tau2_fudge 16) were performed in parallel using a spherical mask covering the TtCST–PolαPrim region (mask2). 427,158 particles from classes with interpretable TtCST–PolαPrim densities were combined after removing duplicates. Refinement of these particles generated a reconstruction with clear TtCST–PolαPrim density. Then, we shifted the centre of each particle to TtCST–PolαPrim and performed signal subtraction using mask4 to only keep the signal from TtCST–PolαPrim. After two rounds of 3D classification using mask4, 142,912 particles were selected and refined using the same mask, which resulted in a 4.2 Å resolution reconstruction for TtCST–PolαPrim (Extended Data Fig. 6b,d). These particles were back projected to original particles without signal subtraction and refined to 4.4 Å resolution for the entire complex including both telomerase and TtCST–PolαPrim.

For the PolαPrim dataset (Extended Data Fig. 7), particle picking was conducted using Topaz[62] in a similar way as described above for the PolαPrim-bound telomerase datasets. After two rounds of 2D classification, 1.3 million particles were selected and refined using an initial model generated by cryoSPARC[63]. The resulting cryo-EM map has a head that is the catalytic core domain of POLA1 and a bow-tie-shaped body that contains POLA2, PRIM1, $PRIM2_N$ and the C-terminal domain of POLA1. The head and the body have multiple orientations relative to each other as indicated by their low-resolution densities in the 3D reconstruction and the 2D classification results (Extended Data Fig. 7b). Focused refinement of the head did not work well owing to its small size, but focused refinement of the body generated a map with clear secondary structure features. After one round of 3D classification using the same mask for the body, 264,498 particles were selected and refined to 4.5 Å resolution. During the 3D classification step, a notable hinge movement was observed within the body. We further refined the two halves of the body individually and obtained a 4.0 Å-resolution reconstruction for POLA2–$POLA1_{CTD}$–$PRIM2_N$ and a 4.3 Å-resolution reconstruction for $PRIM2_N$–PRIM1 (Extended Data Fig. 7c–e).

All cryo-EM maps were sharpened with a negative B-factor and low-pass filtered to the stated resolution using the relion_postprocess program in RELION. Local resolution evaluations were determined by ResMap[64] with two independently refined half-maps. Directional resolution anisotropy analyses were performed using 3DFSC[65]. Data collection and processing statistics are given in Extended Data Table 1.

Model building and refinement

For the modelling of TtCST, two maps were generated from the 3.5 Å resolution cryo-EM reconstruction: an unsharpened map with the best density continuity was used for backbone tracing and secondary structure assignment, and a sharpened map with the best high-resolution features was used to place Cα and side chain of individual residues. Crystal structures of *Tetrahymena* Ten1–Stn1-OB[22,23] (PDB 5DOI and 5DFM) and cryo-EM structure of *Tetrahymena* telomerase-core RNP–TEB–p50[40] (PDB 7LMA) were initially rigid-body fitted into the maps using UCSF Chimera[66], and refined manually in COOT[67]. Density of Ctc1 was traced from its signature C-terminal α helix, and models of OB-C and OB-B were built de novo against the density in COOT. Visible densities of amino acid residues with bulky side chains, such as Phe, Tyr and Trp were used as guidance for sequence assignment (Extended Data Fig. 1g). For Ctc1 OB-A, an initial model was built against the cryo-EM density and refined manually with structure information obtained from NMR (Extended Data Fig. 3). In brief, secondary structure information obtained from

TALOS+[54] was used to define the boundaries of β strands within Ctc1 OB-A (Extended Data Fig. 3d), and 105 inter-β-strand NOE restraints were used to refine the relative position of the β-strands (Extended Data Fig. 3e). Last, p50 residues 184–208 following the C terminus of the previous model of the p50 OBdomain[40] (PDB 7LMA) were built into the cryo-EM map adjacent to Ctc1 OB-A (Extended Data Fig. 1h).

For the modelling of TtCST–PolαPrim, the TtCST model obtained as described above, crystal structures of Stn1 WH–WH[22,23] (PDB 5DFN and 5DOK) and a computed model of $POLA1_{core}$ were generated using AlphaFold2[68] were initially rigid-body fitted into the 4.2 Å resolution map (Extended Data Fig. 6d) using UCSF Chimera[66], and refined manually in COOT[67] (Extended Data Fig. 6h–j). A segment of sstDNA was built manually against the density in the C-shape cleft of Ctc1 OB-C. The previously reported cryo-EM structure of *Tetrahymena* telomerase-core RNP–TEB–p50[40] (PDB 7LMA) was refined against the 2.9 Å-resolution map (Extended Data Fig. 6c).

For the modelling of PolαPrim platform (POLA2–$POLA1_{CTD}$–$PRIM2_N$–PRIM1), a composite cryo-EM density map was generated using the 'combine focused maps' function in Phenix[69] with two focused refined maps (Extended Data Fig. 7a,e). Computed models of individual subunits generated using AlphaFold2[68] were rigid-body fitted into the composite map and refined manually in COOT[67] (Extended Data Fig. 7g).

All models were refined using Phenix[69] in real space with secondary structure, Ramachandran, and rotamer restraints. Refinement statistics of the models are summarized in Extended Data Table 1. Model vs map FSC validations are shown in Extended Data Figs. 1f, 6f and 7f. Structural similarity analyses were conducted using the Dali sever[70]. Sequence alignment results were presented using Jalview[71]. All figures presenting the model were prepared using UCSF ChimeraX[72].

Telomerase–PolαPrim activity assays

The direct telomerase activity assays were carried out as previously described[40] in 20 µl solutions containing 50 mM Tris-HCl pH 8.0, 2 mM Mg^{2+}, 1 mM spermidine, 2 mM TCEP, 200 µM dTTP, 3 µM dGTP, 5 µCi [α-^{32}P]dGTP (Perkin-Elmer, 6000 Ci mmol^{-1}), 20 nM telomerase–PolαPrim and 1 µM $d(GTTGGG)_3$ or $d(GTTGGG)_{10}$ primer as indicated. The C-strand synthesis assay was carried out in 20 µl solutions containing 50 mM Tris-HCl pH 8.0, 2 mM Mg^{2+}, 1 mM spermidine, 2 mM TCEP, 500 µM dATP, 3 µM dCTP, 5 µCi [α-^{32}P]dCTP (Perkin-Elmer, 3000 Ci mmol^{-1}), 0.2 mM ATP, 0.2 mM CTP, 1 µM $d(GTTGGG)_{10}$ primer and 20 nM telomerase–PolαPrim or PolαPrim as indicated. Reactions were performed at 30 °C for 60 min and stopped with quench buffer (10 mM Tris-HCl pH 8.0 and 10 mM EDTA).

The complete telomere replication reactions were carried out in 20 µl solutions containing 50 mM Tris-HCl pH 8.0, 2 mM Mg^{2+}, 1 mM spermidine, 2 mM TCEP, 2 µM dTTP, 3 µM dGTP, 500 µM dATP, 3 µM dCTP, 0.2 mM ATP, 0.2 mM CTP, 1 µM $d(GTTGGG)_3$ primer and 20 nM telomerase–PolαPrim. Either additional 5 µCi [α-^{32}P]dGTP was supplemented to visualize the G-strand synthesis or 5 µCi [α-^{32}P]dCTP was supplemented to visualize the corresponding C-strand synthesis. The reactions were performed at 30 °C and stopped with quench buffer at indicated times. All products were phenol–chloroform-extracted and ethanol-precipitated together with a 15-nt ^{32}P-end-labelled DNA oligonucleotide as a recovery control and resolved on a 10% denaturing polyacrylamide gel. The gels were dried and exposed to a phosphor imaging screen and scanned on an Amersham Typhoon scanner (GE Lifesciences).

Electrophoretic mobility shift assay

EMSAs were conducted following a previously reported method[13]. TtCST and its mutants were expressed and purified from insect cells as described above. For each binding reaction, 0.5 nM ^{32}P-labelled primer (for Extended Data Fig. 9h) or 0.5 nM ^{32}P-labelled primer plus 20 nM unlabelled primer (for Fig. 4e and Extended Data Fig. 9i) was incubated with or without TtCST in 10 µl EMSA buffer (20 mM HEPES-NaOH (pH 8.0), 150 mM NaCl, 2 mM $MgCl_2$, 5% (v/v) glycerol, 50 µg ml^{-1} BSA, 1uM random hexamer (Invitrogen), 0.05% (v/v) Tween-20 and 1 mM TCEP) for 1 h on ice before being loaded onto a 0.5× TBE, 0.7% SeaKem LE agarose (Lonza) gel. The gels were run at 6.8 V cm^{-1} in 0.5× TBE buffer for 40 min and then vacuum dried onto a Hybond-N+ membrane (Cytiva) with 2 pieces of 3MM chromatography paper (Whatman). The gels were exposed to a phosphor imaging screen overnight. The final images were obtained by scanning the screen on an Amersham Typhoon scanner (GE Lifesciences) and then quantified with QuantityOne (Bio-rad). K_D was calculated by fitting the Hill equation using the fraction of protein-bound primer θ: $\theta = P_f^n/(P_f^n + K_D^n)$, $P_f = P_t - (P_t + D_t + K_D - \sqrt{(P_t + D_t + K_D)^2 - 4 \times P_t \times D_t})/2$, where P_f is the unbound protein concentration, P_t is the total protein concentration, D_t is the total DNA concentration, and n is the Hill coefficient. K_D values obtained using the simplified Hill equation ($P_f \approx P_t$) were 2–5% higher.

Statistics and reproducibility

POLA1–POLA2 and its complex with telomerase were successfully purified three times. POLA1–POLA2–PRIM1–PRIM2 and its complex with telomerase were successfully purified more than ten times. TtCST were successfully purified more than three times for the wild type and two times for each Ctc1 variant. Size-exclusion chromatography profiles and protein gels shown in Extended Data Figs. 5a,c,e,f and 9g present representative results. EMSAs of $d(GTTGGG)_5$ DNA binding by wild-type and Ctc1 mutant TtCST shown in Fig. 4e and Extended Data Fig. 9i were successfully repeated three times. EMSAs of variant sstDNA binding by wild-type TtCST shown in Extended Data Fig. 9h were successfully repeated two times. Activity assay results shown in Fig. 3c and Extended Data Fig. 5i,j were successfully repeated three times for each condition.

Reporting summary

Further information on research design is available in the Nature Research Reporting Summary linked to this paper.

Data availability

Cryo-EM density maps have been deposited in the Electron Microscopy Data Bank under accession numbers EMD-26863 (telomerase with CST), EMD-26864 (telomerase with CST–PolαPrim), EMD-26865 (telomerase), EMD-26866 (CST–PolαPrim), EMD-26867 (PolαPrim platform), EMD-26868 (POLA2–$POLA1_{CTD}$–$PRIM2_N$) and EMD-26869 ($PRIM2_N$–PRIM1). The atomic models have been deposited in the Protein Data Bank under accession codes 7UY5 (telomerase with CST), 7UY6 (telomerase), 7UY7 (CST–PolαPrim) and 7UY8 (PolαPrim platform). Backbone chemical shifts have been deposited in BMRB under accession codes 51441 (Ctc1 OB-A), 51442 (Ctc1 OB-A with p50 peptide 228–250) and 51443 (p50 peptide 228–250).

51. Lee, W., Tonelli, M. & Markley, J. L. NMRFAM-SPARKY: enhanced software for biomolecular NMR spectroscopy. *Bioinformatics* **31**, 1325–1327 (2015).
52. Herrmann, T., Guntert, P. & Wuthrich, K. Protein NMR structure determination with automated NOE-identification in the NOESY spectra using the new software ATNOS. *J. Biomol. NMR* **24**, 171–189 (2002).
53. Guntert, P. & Buchner, L. Combined automated NOE assignment and structure calculation with CYANA. *J. Biomol. NMR* **62**, 453–471 (2015).
54. Shen, Y., Delaglio, F., Cornilescu, G. & Bax, A. TALOS+: a hybrid method for predicting protein backbone torsion angles from NMR chemical shifts. *J. Biomol. NMR* **44**, 213–223 (2009).
55. Shen, Y. et al. Consistent blind protein structure generation from NMR chemical shift data. *Proc. Natl Acad. Sci. USA* **105**, 4685–4690 (2008).
56. Williamson, M. P. Using chemical shift perturbation to characterise ligand binding. *Prog. Nucl. Magn. Reson. Spectrosc.* **73**, 1–16 (2013).
57. Jiang, J. et al. The architecture of *Tetrahymena* telomerase holoenzyme. *Nature* **496**, 187–192 (2013).
58. Mastronarde, D. N. Automated electron microscope tomography using robust prediction of specimen movements. *J. Struct. Biol.* **152**, 36–51 (2005).
59. Zivanov, J. et al. New tools for automated high-resolution cryo-EM structure determination in RELION-3. *eLife* **7**, e42166 (2018).
60. Zheng, S. Q. et al. MotionCor2: anisotropic correction of beam-induced motion for improved cryo-electron microscopy. *Nat. Methods* **14**, 331–332 (2017).

61. Rohou, A. & Grigorieff, N. CTFFIND4: Fast and accurate defocus estimation from electron micrographs. *J. Struct. Biol.* **192**, 216–221 (2015).
62. Bepler, T. et al. Positive-unlabeled convolutional neural networks for particle picking in cryo-electron micrographs. *Nat. Methods* **16**, 1153–1160 (2019).
63. Punjani, A., Rubinstein, J. L., Fleet, D. J. & Brubaker, M. A. cryoSPARC: algorithms for rapid unsupervised cryo-EM structure determination. *Nat. Methods* **14**, 290–296 (2017).
64. Kucukelbir, A., Sigworth, F. J. & Tagare, H. D. Quantifying the local resolution of cryo-EM density maps. *Nat. Methods* **11**, 63–65 (2014).
65. Tan, Y. Z. et al. Addressing preferred specimen orientation in single-particle cryo-EM through tilting. *Nat. Methods* **14**, 793–796 (2017).
66. Pettersen, E. F. et al. UCSF Chimera—a visualization system for exploratory research and analysis. *J. Comput. Chem.* **25**, 1605–1612 (2004).
67. Emsley, P., Lohkamp, B., Scott, W. G. & Cowtan, K. Features and development of Coot. *Acta Crystallogr. D* **66**, 486–501 (2010).
68. Jumper, J. et al. Highly accurate protein structure prediction with AlphaFold. *Nature* **596**, 583–589 (2021).
69. Adams, P. D. et al. PHENIX: a comprehensive Python-based system for macromolecular structure solution. *Acta Crystallogr. D* **66**, 213–221 (2010).
70. Holm, L. Using Dali for protein structure comparison. *Struct. Bioinformatics* **2112**, 29–42 (2020).
71. Waterhouse, A. M., Procter, J. B., Martin, D. M., Clamp, M. & Barton, G. J. Jalview Version 2—a multiple sequence alignment editor and analysis workbench. *Bioinformatics* **25**, 1189–1191 (2009).
72. Goddard, T. D. et al. UCSF ChimeraX: meeting modern challenges in visualization and analysis. *Protein Sci.* **27**, 14–25 (2018).
73. Baranovskiy, A. G. et al. Structural basis for inhibition of DNA replication by aphidicolin. *Nucleic Acids Res.* **42**, 14013–14021 (2014).
74. Perera, R. L. et al. Mechanism for priming DNA synthesis by yeast DNA polymerase α. *eLife* **2**, e00482 (2013).

Acknowledgements This work was supported by grants from NIH R35GM131901 and NSF MCB2016540 to J.F. and NIH R01GM071940 to Z.H.Z. We acknowledge the use of instruments at the Electron Imaging Center for Nanomachines supported by UCLA and instrumentation grants from NIH (1S10OD018111 and U24GM116792) and NSF (DBI-1338135 and DMR-1548924). The UCLA-DOE NMR core facility is supported in part by US Department of Energy grant DE-AC02-06CH11357 and NIH instrumentation grants S10OD016336 and S10OD025073.

Author contributions Y.H. and H.S. prepared and checked electron microscopy samples. Y.H. collected and analysed cryo-EM data. Y.H. and H.S. built the models. H.C. expressed and purified samples for NMR analysis. H.C., Y.W. and L.S. collected and analysed NMR data. H.S. and B.L. conducted activity assays. B.L. and Y.H. conducted EMSA assays. Z.H.Z. supervised cryo-EM data collection and processing. J.F. supervised all aspects of the project. Y.H. and J.F. made figures and wrote the manuscript, with input from H.S., Y.W. and B.L.

Competing interests The authors declare no competing interests.

Additional information

Supplementary information The online version contains supplementary material available at https://doi.org/10.1038/s41586-022-04931-7.

Correspondence and requests for materials should be addressed to Juli Feigon.

Peer review information *Nature* thanks the anonymous reviewers for their contribution to the peer review of this work. Peer review reports are available.

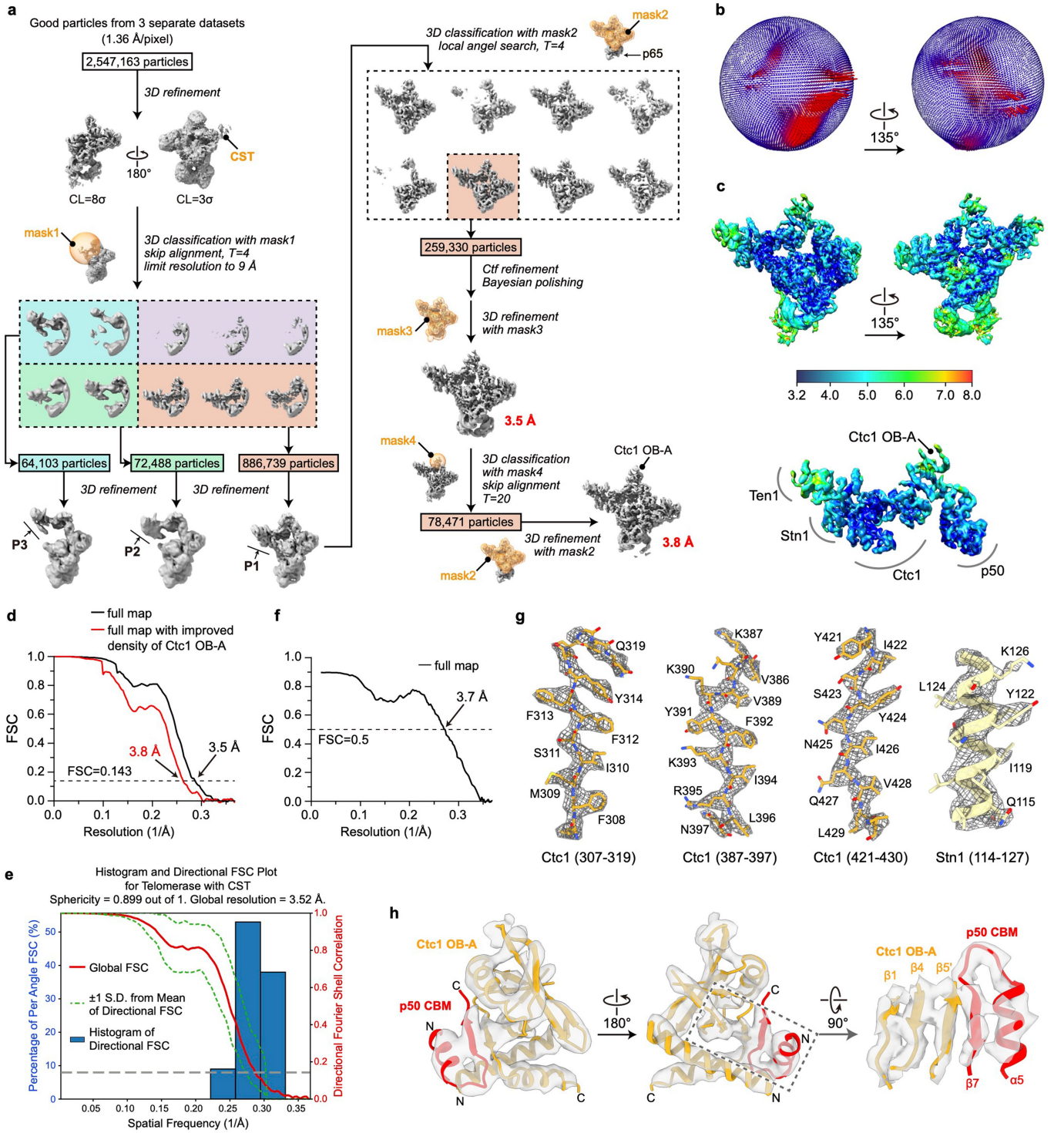

Extended Data Fig. 1 | Cryo-EM data processing workflow of TtCST in telomerase holoenzyme and evaluations of the final reconstructions. **a**, Data processing workflow (detailed in Methods). **b**, Euler angle distributions of particles used for the final 3.5 Å resolution reconstruction. **c**, Local resolution evaluation of the 3.5 Å resolution reconstruction shown for the overall map (upper) and for the TtCST–p50 region (lower). **d**, Plot of the Fourier shell correlation (FSC) as a function of the spatial frequency demonstrating the resolutions of final reconstructions. **e**, 3D FSC analysis[65] of the 3.5 Å resolution reconstruction. Shown are the global FSC (red line), the spread of directional resolution values (area encompassed by the green dotted lines) and the histogram of directional resolutions evenly sampled over the 3D FSC (blue bars). A sphericity (0.5 threshold) of 0.899 indicates almost isotropic angular distribution of resolution (a value of 1 stands for completely isotropic angular distribution). **f**, FSC coefficient as a function of spatial frequency between model and cryo-EM density map. **g**, Representative cryo-EM densities (grey and mesh) encasing the related atomic models (coloured sticks and ribbons). **h**, Superimposition of cryo-EM densities (low-pass filtered to 5 Å) and model of Ctc1 OB-A in complex with p50 CBM.

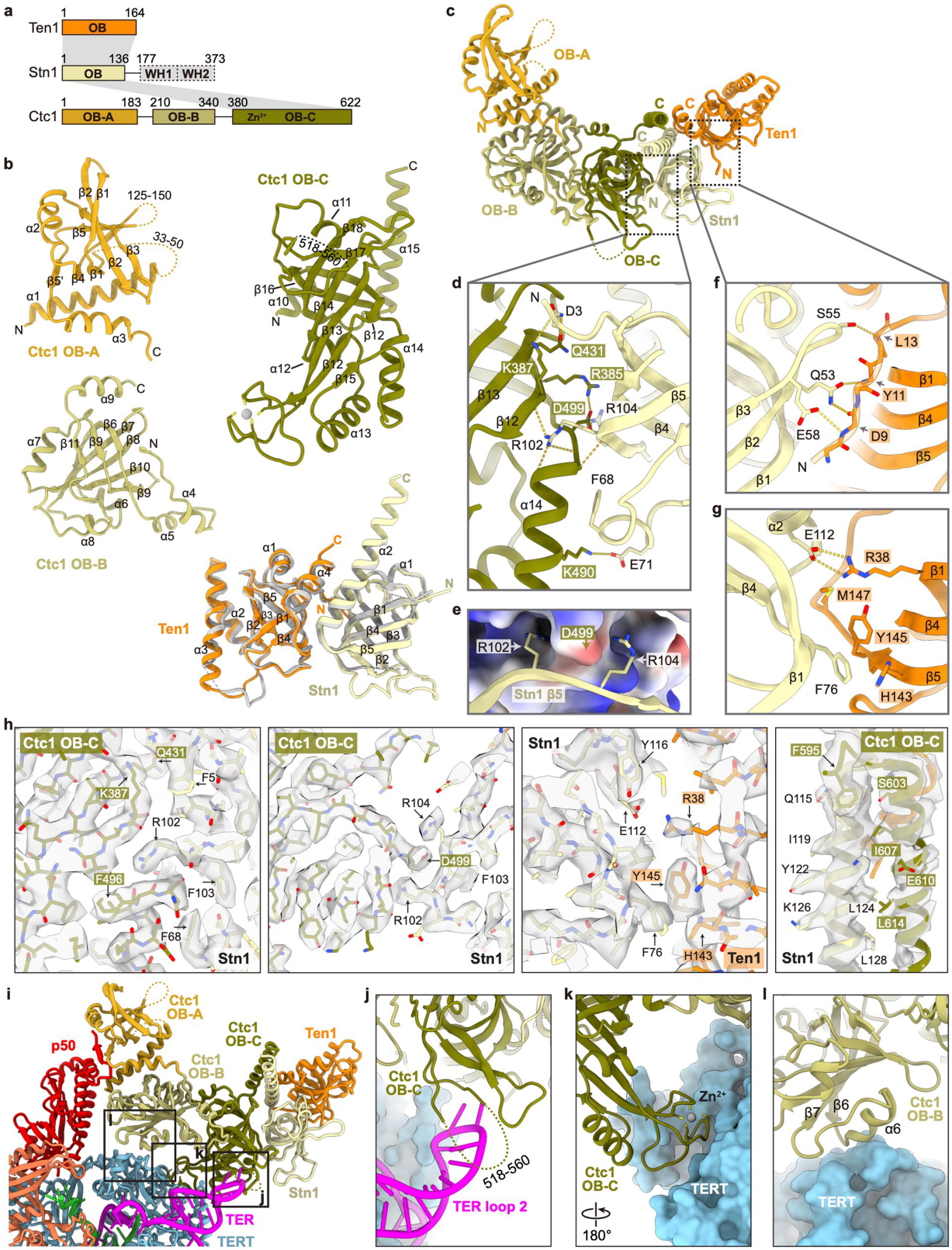

Extended Data Fig. 2 | See next page for caption.

Extended Data Fig. 2 | Structural details of TtCST. a, Domain organization of TtCST subunits. Invisible regions in the cryo-EM map are shown as dashed boxes. Intermolecular interactions are indicated as grey shading. **b**, Ribbon diagrams of TtCST subunits/domains with secondary-structure elements labelled. Unmodelled regions are shown as dashed lines. Crystal structure of Ten1–Stn1 OB[23] (PDB 5DOI) is shown in grey and overlaid with the cryo-EM structure for comparison. **c**, Ribbon representation of TtCST structure with individual OB domain coloured as indicated. **d**, Close-up view of the interface between Ctc1 OB-C and Stn1 OB. Salt bridge and hydrogen-bonding interactions are shown as dashed yellow lines. **e**, Two arginine sidechains on Stn1 OB (ribbon) clamp D499 on Ctc1 OB-C (electrostatic surface). **f**, **g**, Detailed interactions between Stn1 OB and Ten1. **h**, Close-up views of the cryo-EM densities of the interfaces between CST subunits (Fig. 1e, Extended Data Fig. 2d–g). **i**, Overall view of the interface between TtCST and TERT–TER. **j**–**l**, Close-up views of interactions between TtCST and TERT–TER as indicated in dashed boxes in **h**. These interactions stabilize TtCST in the predominant conformation.

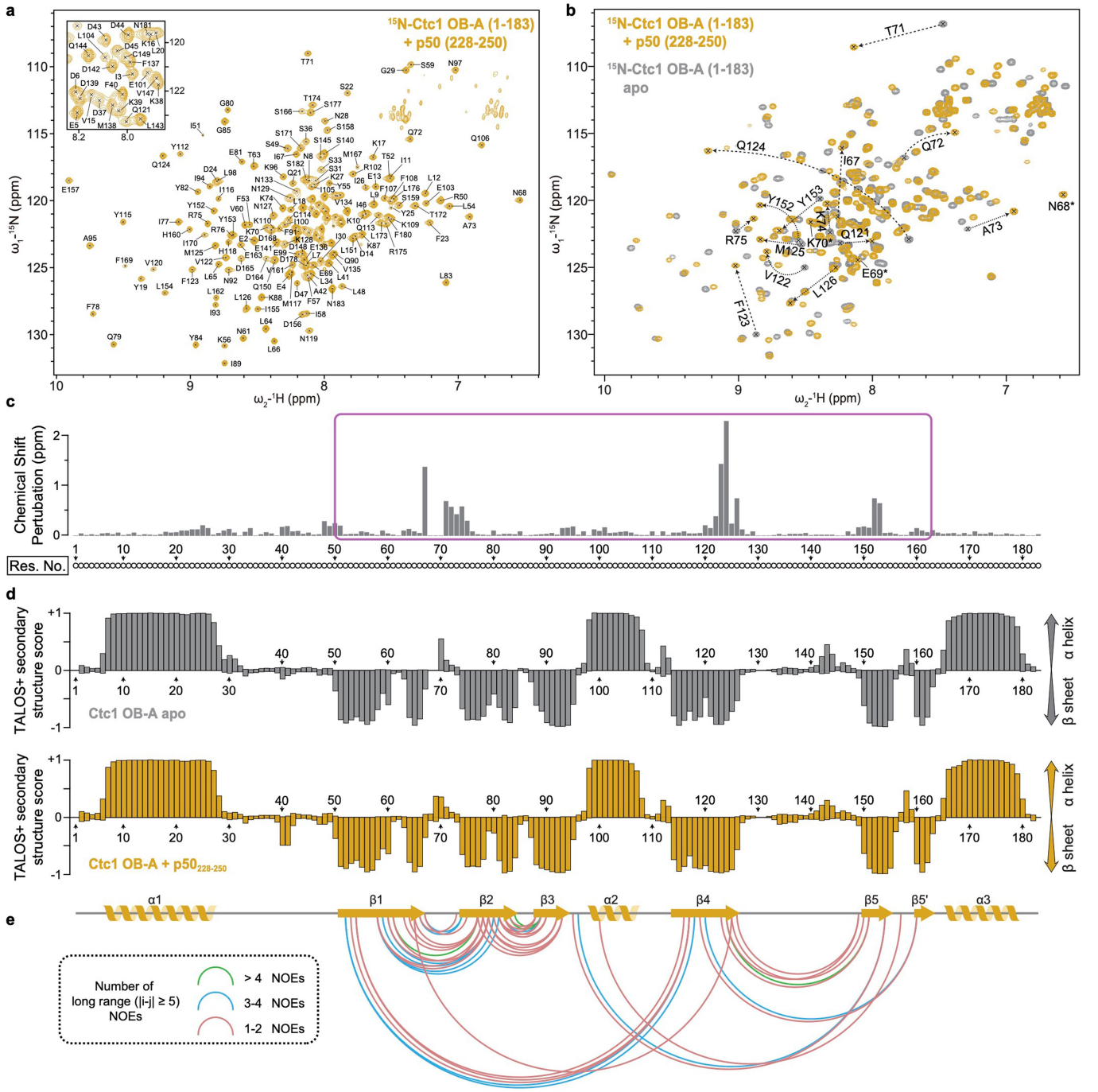

Extended Data Fig. 3 | NMR spectra and structural study of Ctc1 OB-A with p50 peptide. a, Assigned ^{1}H-^{15}N HSQC spectrum of ^{15}N-labelled Ctc1 OB-A (residues 1-183) in the presence of unlabelled p50 peptide (residues 228-250). Inset shows the expanded central region of the spectrum. **b**, Superimposed ^{1}H-^{15}N HSQC spectra of ^{15}N-labelled Ctc1 OB-A in the presence (yellow) and absence (gray) of unlabelled p50 peptide. Signals from the same residues with chemical shift differences of more than 0.25 ppm are connected by dashed arrows. Signals from residues 68-70 that only appear in the presence of p50 peptide are labelled with asterisks. **c**, Chemical shift perturbation (CSP) index of ^{15}N-labelled Ctc1 OB-A upon binding p50 peptide. Magenta box indicates the region that is shown in Fig. 2d. **d**, Chemical-shift-based secondary-structure score of Ctc1 OB-A in the absence (grey) and presence (yellow) of p50 peptide. The scores are determined using TALOS+ (ref. [54]). Top and bottom edges of each bar represent the probabilities of each residue assigned to be α helix and β sheet, respectively. The secondary structure of Ctc1 OB-A observed in the cryo-EM structure is shown below for comparison. **e**, Plot of long range (greater than 5 residues) ^{1}H-^{1}H NOE restraints observed within Ctc1 OB-A. Residues with pairwise NOE restraint(s) are connected by a link. Links are colour coded as indicated based on the number of NOE restraints between the two connected residues.

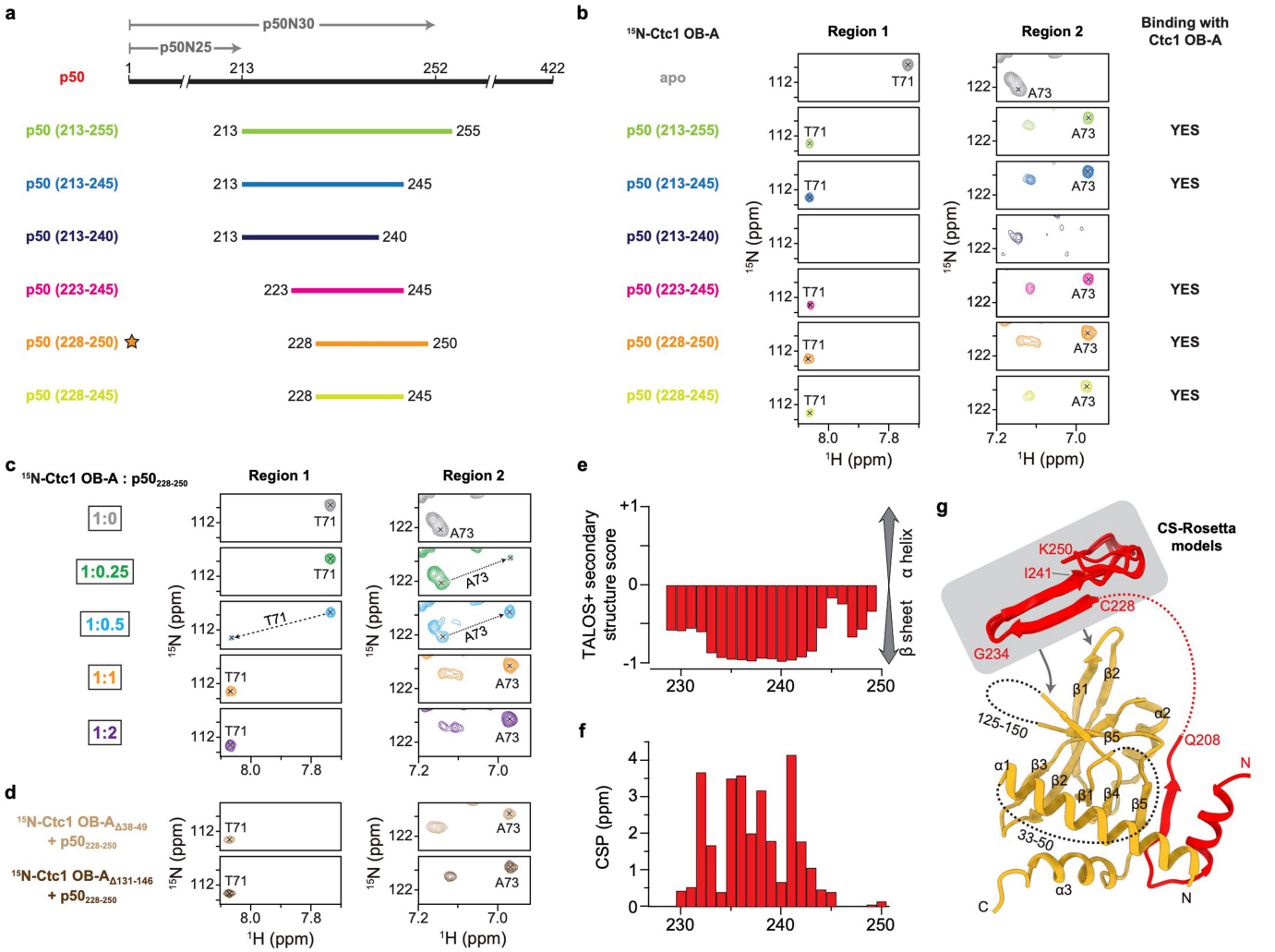

Extended Data Fig. 4 | Identifying the 'invisible' interface between Ctc1 OB-A and p50 peptide using NMR methods. a, Schematic diagram of p50 and constructs of p50 peptide. The N-terminal 30 kDa and 25 kDa fragments of p50 are labelled as p50N30 and p50N25, respectively. Previous biochemical study showed that p50N30 could bind Ctc1, whereas p50N25 could not[43]. The cryo-EM structure of p50 ends at residue 208 (Fig. 2b). On the basis of these facts, a series of p50 peptides in the range of residues 213-255 were designed to explore additional interface between p50 and Ctc1 OB-A that are 'invisible' in the cryo-EM structure. **b**, NMR binding study of p50 peptides with Ctc1 OB-A. Two regions of ^{1}H-^{15}N HSQC spectra of ^{15}N-labelled Ctc1 OB-A in the absence (apo) and presence of unlabelled p50 peptides were shown. Chemical shifts of T71 and A73 were chosen to illustrate the binding process in this and the following panels, **c** and **d**. $p50_{228\text{-}250}$ peptide is determined to be the optimal construct and was used for other NMR studies presented here. **c**, Titration series of p50 peptide into ^{15}N-labelled Ctc1 OB-A. The binding is in the slow exchange regime and saturated at 1:1 stoichiometry. **d**, Truncations of two unstructured loops (residues 38-49 and 131-146) of Ctc1 OB-A individually have no effect on its binding with p50 peptide. **e**, Secondary-structure score of $p50_{228\text{-}250}$ in the presence of Ctc1 OB-A. **f**, CSP index of p50 peptide upon binding Ctc1 OB-A. ^{1}H-^{15}N HSQC spectra shown in Fig. 2c were used for the CSP calculation. **g**, Model of the interactions between Ctc1 OB-A and p50. CS-Rosetta models of $p50_{228\text{-}250}$ are shown in the grey box with arrows pointing to the binding surface on Ctc1 OB-A. Unstructured linkers are shown as dashed lines.

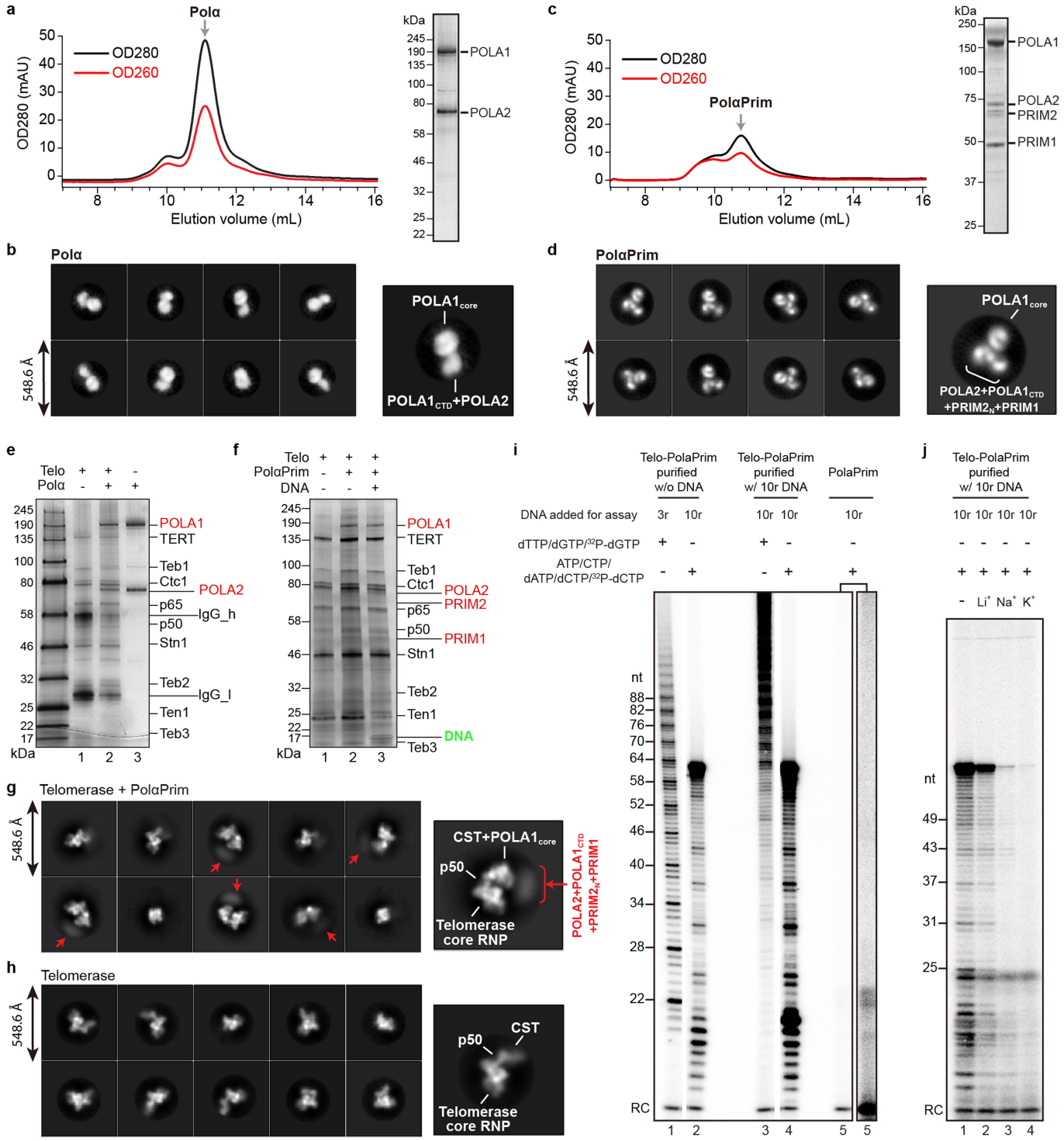

Extended Data Fig. 5 | See next page for caption.

Extended Data Fig. 5 | Characterization of purified *Tetrahymena* PolαPrim samples and their assembly with telomerase holoenzyme. a, Size-exclusion chromatography (SEC) profile (left) and SDS-PAGE gel (right) of Polα. **b**, Representative 2D-class averages of Polα particles obtained from negative-stain EM images. **c**, SEC profile (left) and SDS-PAGE gel (right) of PolαPrim. **d**, Representative 2D-class averages of PolαPrim particles obtained from negative-stain EM images. **e**, Silver-stained SDS-PAGE gel of affinity purified telomerase–Polα (lane 2) shows that Polα can bind telomerase in the absence of Primase. Telomerase (lane 1) and Polα (lane 3) samples were loaded on the same gel for comparison. **f**, Silver-stained SDS-PAGE gel of affinity purified telomerase–PolαPrim samples shows assembly of the complex with or without sstDNA. **g**, Representative 2D-class averages of affinity purified telomerase–PolαPrim obtained from negative-stain EM images. Densities are assigned on the basis of the cryo-EM structure (Fig. 3a) obtained with the same batch of sample. Smeared densities (red arrows) are observed near $POLA1_{core}$ in several classes, so we were able to assign them to the PolαPrim platform, which comprises POLA2, $POLA1_{CTD}$, $PRIM2_{N}$, and PRIM1. **h**, Representative 2D-class averages of telomerase particles shown for comparison with **g**. **i**, Activity assays of telomerase-PolαPrim (lanes 1-4) and PolαPrim alone (lane 5). Direct telomerase activity assays were conducted for G-strand synthesis alone in the presence of dTTP and dGTP (lanes 1 and 3). PolαPrim activity assays were conducted for C-strand synthesis alone in the presence of ATP, CTP, dATP and dCTP (lanes 2, 4 and 5). ^{32}P-dGTP and ^{32}P-dCTP were used to label the G-strand and C-strand products, respectively. A longer exposure is shown for lane 5 so that products can be seen. RC, recovery control. All lanes are from a single gel. **j**, Activity assays of C-strand synthesis (lane 1) relative to that in 50 mM LiCl (lane 2), 50 mM NaCl (lane 3), or 50 mM KCl (lane 4). For lanes 2-4, the DNA templates were incubated in assay buffer containing 50 mM of the indicated cations on ice for 30 min before the reaction.

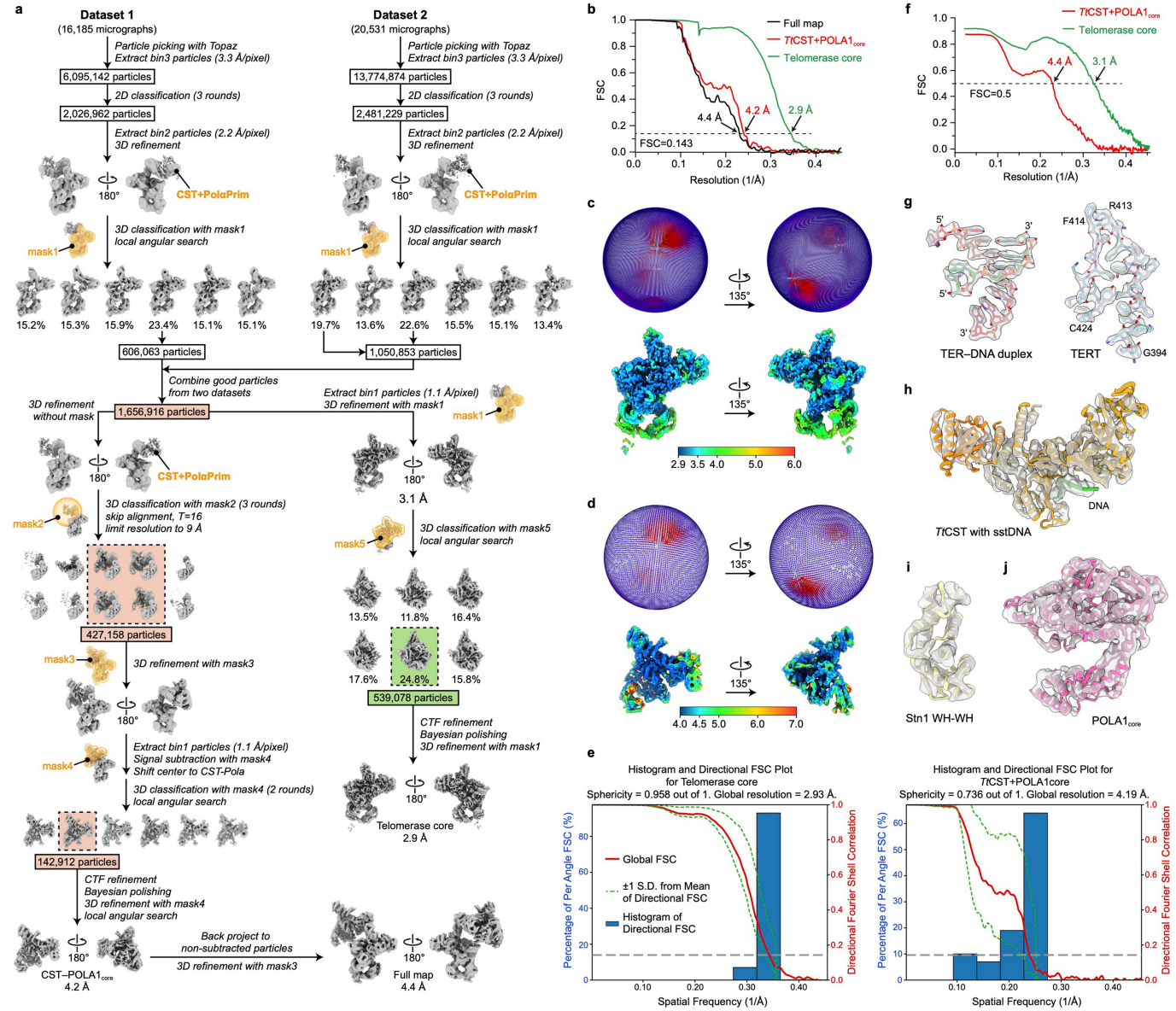

Extended Data Fig. 6 | Cryo-EM structure determination of *Tetrahymena* telomerase–PolαPrim complex. a, Data-processing workflow (detailed in Methods). **b**, Resolution of final reconstructions determined by gold-standard FSC at the 0.143 criterion. **c**, Particle distribution (upper) and local resolution evaluation (lower) of the 2.9 Å resolution reconstruction of telomerase core. **d**, Particle distribution (upper) and local resolution evaluation (lower) of the 4.2 Å resolution reconstruction of TtCST–POLA1$_{core}$. **e**, 3D FSC analysis[65] of the 2.9 Å resolution reconstruction of telomerase core (left) and the 4.2 Å resolution reconstruction of TtCST–POLA1$_{core}$ (right). For each reconstruction, the global FSC (red line), the spread of directional resolution values (area encompassed by the green dotted lines) and the histogram of directional resolutions evenly sampled over the 3D FSC (blue bars) are shown. A sphericity of 0.958 was determined for telomerase core (left), indicating almost isotropic angular distribution of resolution. A sphericity of 0.736 was determined for TtCST-POLA1$_{core}$ (right), suggesting slightly anisotropic angular distribution of resolution. **f**, FSC curves for refined models versus the corresponding cryo-EM density maps. **g**-**j**, Representative cryo-EM densities (transparency surface) encasing the related atomic models (colour sticks and ribbons) for telomerase-core RNP (**g**), CST (**h**), Stn1 WH-WH (**i**) and POLA1$_{core}$ (**j**).

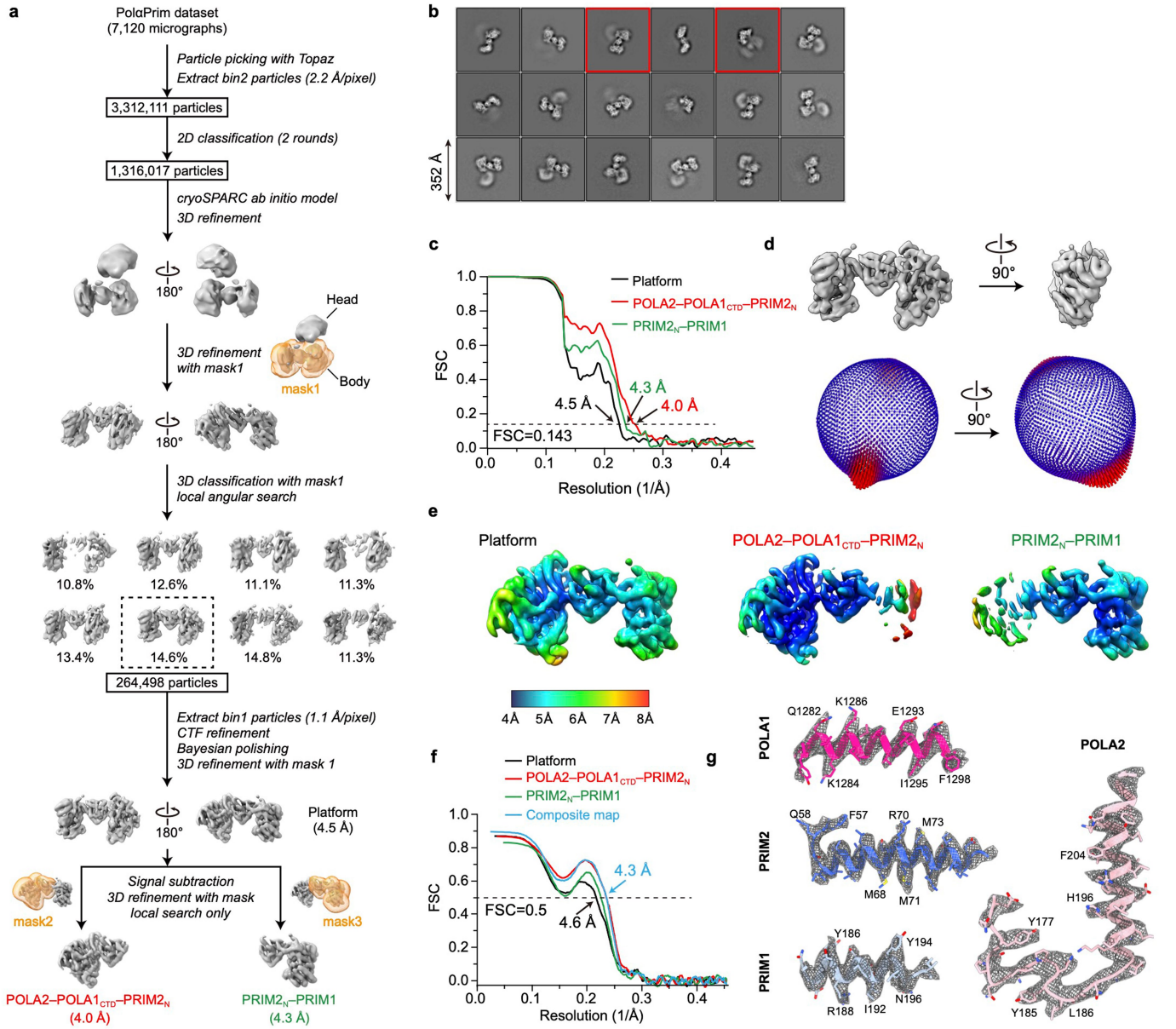

Extended Data Fig. 7 | Cryo-EM structure determination of PolαPrim. **a**, Data processing workflow (detailed in Methods). **b**, Representative 2D-class averages of PolαPrim particles obtained from cryo-EM images. The two classes shown in Fig. 3e are labelled with red boxes. **c**, Resolution of final reconstructions determined by gold-standard FSC at the 0.143 criterion. **d**, Euler angle distributions of particles used for the final reconstructions. **e**, Local resolution evaluations of the final reconstructions. **f**, FSC coefficients as a function of spatial frequency between model and cryo-EM density maps. The composite map is generated using Phenix[69] with two focused refined maps (detailed in Methods). For the full map and the composite map, the complete model was used to calculate the FSCs. For the two focused refined maps, only corresponding regions of the model were used to calculate the FSCs. **g**, Representative cryo-EM densities (grey mesh) encasing the related atomic models (coloured sticks and ribbons).

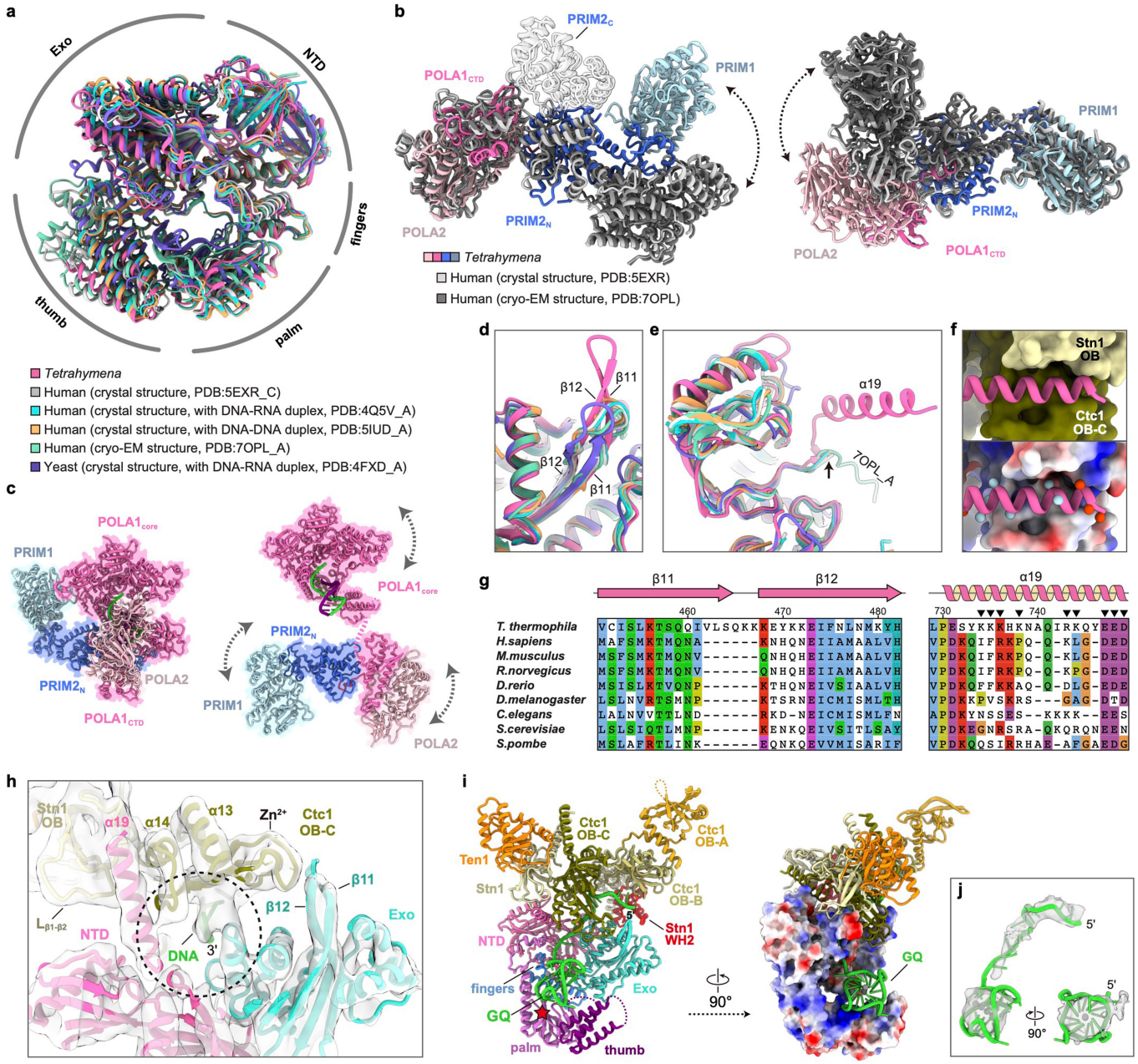

Extended Data Fig. 8 | Structural conservation of *Tetrahymena* PolαPrim. **a**, Superposition of *Tetrahymena* (*Tt*), human and yeast POLA1$_{core}$ structures[45–47,73,74] shown in an overall view. **b**, Structural comparison of PolαPrim platform of *Tt* and human[45,46]. The structures were superposed based on POLA2–POLA1$_{CTD}$ (left) or PRIM1 (right). Arrows indicate dynamics of the unaligned regions. PRIM2$_C$ in human structures are shown as transparent ribbons. PRIM2$_C$ is not observed in the *Tt* structure. **c**, Structures of PolαPrim in an autoinhibited conformation (left, modelled on the basis of PDB 5EXR[45]) and an active conformation (right, modelled on the basis of a low-resolution cryo-EM map in Extended Data Fig. 7a). The DNA-DNA duplexes on POLA1$_{core}$ were modelled on the basis of PDB 5IUD[47]. In the autoinhibited conformation (left), the active site on POLA1$_{core}$ is sterically blocked by POLA1$_{CTD}$ and POLA2 for DNA entry. In the active conformation (right), dynamics of subunits are indicated with arrows. **d-e**, Superposition of *Tt*, human and yeast POLA1$_{core}$ structures for the regions that are on the interface with TtCST. Conserved domains/motifs are labeled as indicated. The β11-β12 hairpin in *Tt* POLA1$_{core}$ is longer than those in human and yeast (**d**). The α19 is structured only in *Tt* POLA1 when binding TtCST (**e**). **f**, Close-up views of the interface between *Tt* POLA1$_{core}$ α19 (ribbon) and TtCST (surface/electrostatic surface). In the lower panel, locations of positively and negatively charged residues on α19 are indicated using blue and red balls, respectively. **g**, Sequence-conservation analysis of the β11-β12 hairpin and α19 of POLA1. Charged residues on α19 are indicated with black arrows. **h**, Close-up view of the interface between POLA1$_{core}$ and TtCST with sstDNA. Cryo-EM densities are shown as transparent surface. The template entry port formed by POLA1$_{core}$ NTD and Exo and Ctc1 OB-C is indicated by a cycle. **i**, Path of sstDNA in the cryo-EM structure of *Tt* telomerase–PolαPrim. The sstDNA binds in the C-shape cleft of Ctc1 OB-C with its 5' side, while its 3' side passes through the template entry port to the active site of POLA1$_{core}$ (left). A G-quadruplex (GQ) formed by four *Tt* telomere repeats (modelled on the basis of PDB 7JKU[48]) is observed on a positively charged DNA binding surface of POLA1$_{core}$ between the palm and thumb (right). **j**, Superimposition of the GQ structure and cryo-EM density. Weak density of sstDNA can be observed connecting the sstDNA on Ctc1 OB-C to the GQ.

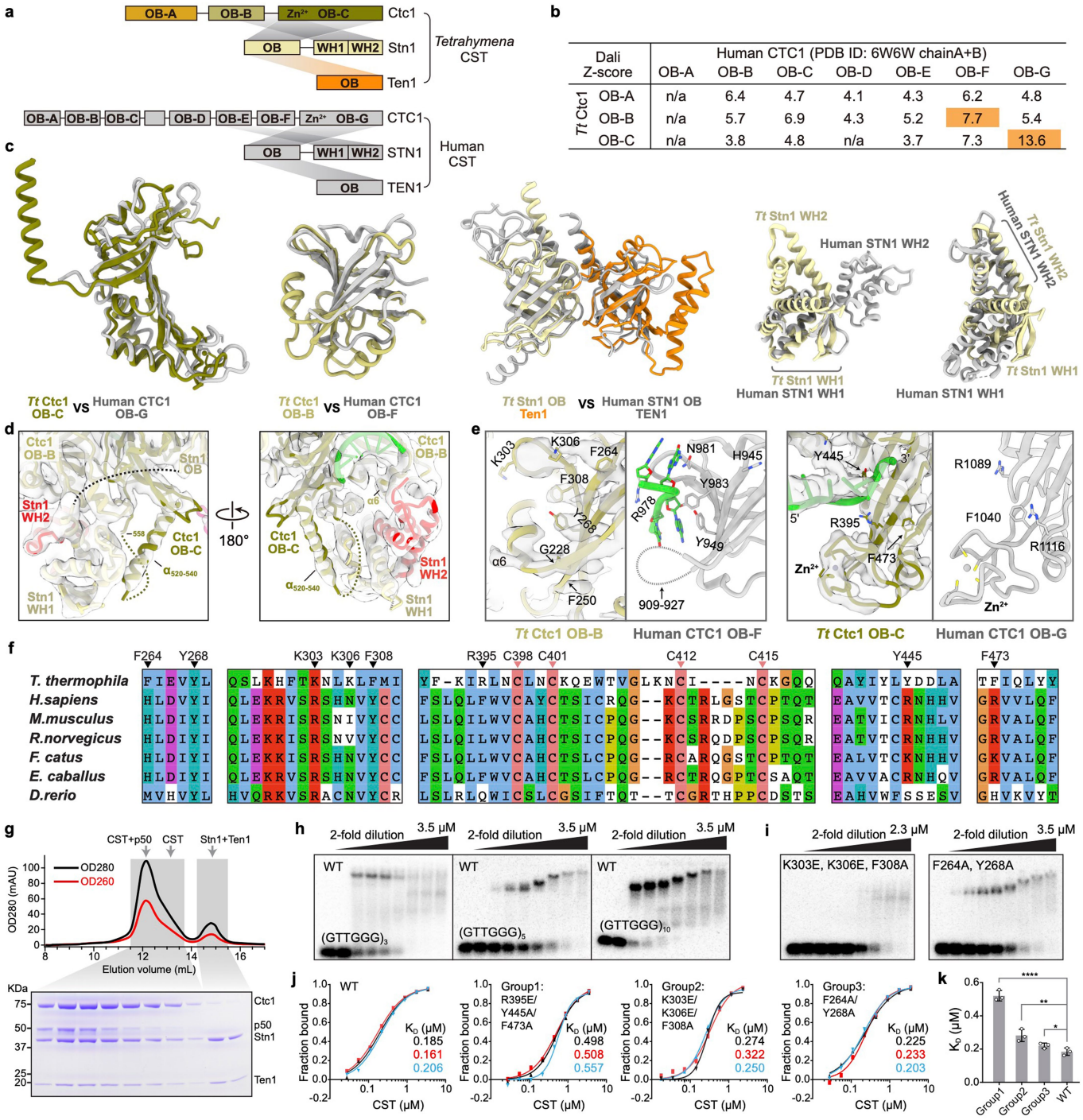

Extended Data Fig. 9 | See next page for caption.

Extended Data Fig. 9 | Comparison of TtCST and human CST. a, Domain diagrams of TtCST and human CST. **b**, Structural homology analysis of individual OB domains of *Tt*Ctc1 (OB-A to -C) and human CTC1 (OB-A to -G) using the Dali sever[70]. On the basis of the resulted pairwise Z-scores, *Tt*Ctc1 OB-B and OB-C are identified as homologues of human CTC1 OB-F and OB-G, respectively. **c**, Structural comparison of individual domains from TtCST (colour) with corresponding domains from human CST (grey). Structures of WH-WH domains of *Tt* Stn1 and human STN1 were superposed based on WH1 or WH2 domain. The relative orientation of the two WH domains is different between *Tt* and human. **d**, The interface between Stn1 WH-WH and Ctc1 in the cryo-EM structure of *Tt* telomerase–PolαPrim. Cryo-EM densities are shown as transparent surfaces. An previously unstructured loop of Ctc1 OB-C (Extended Data Fig. 2b) partially forms an α helix ($\alpha_{520\text{-}540}$) and contributes to the interface with Stn1 WH-WH. **e**, Comparison of DNA binding sites on *Tt*Ctc1 (colour) and human CTC1 (grey). Conserved residues located on the DNA binding interface are shown as sticks. Cryo-EM densities of *Tt*Ctc1 are shown as transparent surfaces. In the decameric structure of human CST[19] (PDB 6W6W), sstDNA primarily binds on CTC1 OB-F. However, in TtCST, the equivalent sstDNA binding site on OB-B is partially occluded by a helix (α6) that is part of an unstructured loop in hCTC1 OB-F. The helix α6 abuts TERT in TtCST without PolαPrim (Extended Data Fig. 2k) and Stn1 WH2 when PolαPrim is bound (as shown in **d**). **f**, Sequence conservation analysis of Ctc1 residues on the DNA binding interface. Residues shown in **e** are indicated with black arrows. Conserved cysteines in the zinc ribbon motifs are indicated with pink arrows. **g**, SEC profile and SDS-PAGE gel of TtCST–p50 co-expressed in Sf9 cells. Gel samples are from the peak fractions of the SEC profile as indicated. **h**, EMSA of purified wild-type TtCST with $d(GTTGGG)_n$, where n = 3, 5 or 10. **i**, Substitutions of *Tt*Ctc1 OB-B conserved residues K303E/K306E/F308A and F264A/Y268A substantially decrease $d(GTTGGG)_5$ binding, as indicated by EMSAs. These results suggest that the binding site on *Tt*Ctc1 OB-B might be accessible to sstDNA in free TtCST where neither TERT nor Stn1 WH-WH stabilize helix α6. Wedges indicate two-fold dilution of TtCST. The first lane of each gel is a TtCST-free control. **j**, Quantifications of fraction of bound DNA for all the independent EMSA experiments with TtCST WT and variants as indicated (n = 3 biological replicates). K_D values were determined as described in Methods. **k**, Effect of TtCST residue substitutions on $d(GTTGGG)_5$ binding. Data are mean ± s.d. from n = 3 biological replicates shown in **j**. **P* = 0.04, ***P* = 0.009, *****P* < 0.0001; one-tailed unpaired t-tests.

Extended Data Table 1 | Cryo-EM data collection, refinement and validation statistics

	Telomerase with CST (EMD-26863) (PDB 7UY5)	Telomerase with CST–PolαPrim (EMD-26864)	Telomerase (EMD-26865) (PDB 7UY6)	CST–PolαPrim (EMD-26866) (PDB 7UY7)	PolαPrim platform (EMD-26867) (PDB 7UY8)	POLA2–POLA1$_{CTD}$–PRIM2$_N$ (EMD-26868)	PRIM2$_N$–PRIM1 (EMD-26869)
Data collection and processing							
Magnification	105,000	81,000	81,000	81,000	81,000	81,000	81,000
Voltage (kV)	300	300	300	300	300	300	300
Electron exposure (e–/Å^2)	48	55	55	55	55	55	55
Defocus range (μm)	−0.8 – −4.0	−0.8 – −4.0	−0.8 – −4.0	−0.8 – −4.0	−0.8 – −4.0	−0.8 – −4.0	−0.8 – −4.0
Pixel size (Å)	1.36	1.1	1.1	1.1	1.1	1.1	1.1
Symmetry imposed	C1	C1	C1	C1	C1	C1	C1
Initial particle images (no.)	2,547,163	19,870,016	19,870,016	19,870,016	3,312,111	3,312,111	3,312,111
Particle images after class2d (no.)	n/a	4,508,191	4,508,191	4,508,191	1,316,017	1,316,017	1,316,017
Final particle images (no.)	259,330	142,912	539,078	142,912	264,498	264,498	264,498
Map resolution (Å)	3.5	4.4	2.9	4.2	4.5	4.0	4.3
FSC threshold	0.143	0.143	0.143	0.143	0.143	0.143	0.143
Map resolution range (Å)	3.2 – 6.0	4.0 – 7.0	2.9 – 5.0	4.0 – 7.0	4.0 – 7.0	4.0 – 6.0	4.0 – 6.0
Refinement							
Initial model used (PDB code)	7LMA, 5DOI, 5DFM		7LMA	7UY5, 5DFN, 5DOK, AlphaFold2	AlphaFold2		
Model resolution (Å)	3.7		3.1	4.4	4.3		
FSC threshold	0.5		0.5	0.5	0.5		
Map sharpening *B* factor (Å^2)	-130		-80	-100	-100		
Model composition							
Non-hydrogen atoms	25,772		18,746	15,161	9,552		
Protein residues	2,690		1,847	1,808	1,161		
RNA/DNA Nucleotides	170		170	10	0		
Ligands	2		1	1	1		
B factors (Å^2)							
Protein	21.8		47.5	124.3	74.4		
RNA/DNA/Ligands	82.6		147.8	150.5	180.8		
R.m.s. deviations							
Bond lengths (Å)	0.002		0.002	0.002	0.003		
Bond angles (°)	0.455		0.442	0.557	0.636		
Validation							
MolProbity score	1.54		1.19	1.91	1.87		
Clashscore	7.03		4.00	13.86	8.69		
Poor rotamers (%)	0.04		0.00	0.18	0.00		
Ramachandran plot							
Favored (%)	97.17		98.30	96.17	93.92		
Allowed (%)	2.83		1.70	3.83	6.08		
Disallowed (%)	0.00		0.00	0.00	0.00		

nature research

Corresponding author(s): Juli Feigon

Last updated by author(s): May 12, 2022

Reporting Summary

Nature Research wishes to improve the reproducibility of the work that we publish. This form provides structure for consistency and transparency in reporting. For further information on Nature Research policies, see our Editorial Policies and the Editorial Policy Checklist.

Statistics

For all statistical analyses, confirm that the following items are present in the figure legend, table legend, main text, or Methods section.

n/a	Confirmed	
☐	☒	The exact sample size (*n*) for each experimental group/condition, given as a discrete number and unit of measurement
☐	☒	A statement on whether measurements were taken from distinct samples or whether the same sample was measured repeatedly
☐	☒	The statistical test(s) used AND whether they are one- or two-sided *Only common tests should be described solely by name; describe more complex techniques in the Methods section.*
☒	☐	A description of all covariates tested
☒	☐	A description of any assumptions or corrections, such as tests of normality and adjustment for multiple comparisons
☐	☒	A full description of the statistical parameters including central tendency (e.g. means) or other basic estimates (e.g. regression coefficient) AND variation (e.g. standard deviation) or associated estimates of uncertainty (e.g. confidence intervals)
☐	☒	For null hypothesis testing, the test statistic (e.g. *F*, *t*, *r*) with confidence intervals, effect sizes, degrees of freedom and *P* value noted *Give P values as exact values whenever suitable.*
☒	☐	For Bayesian analysis, information on the choice of priors and Markov chain Monte Carlo settings
☒	☐	For hierarchical and complex designs, identification of the appropriate level for tests and full reporting of outcomes
☒	☐	Estimates of effect sizes (e.g. Cohen's *d*, Pearson's *r*), indicating how they were calculated

Our web collection on statistics for biologists contains articles on many of the points above.

Software and code

Policy information about availability of computer code

Data collection	SerialEM3.8, Topspin4.1
Data analysis	RELION3.1, cryoSPARC_v3.2, MotionCor2 1.2.1, CTFFIND 4.1.14, Topaz0.2.4, ResMap1.1.4, Coot0.8.9, UCSF Chimera 1.16 and ChimeraX 1.2, PHENIX1.19, QuantityOne 4.6.2, Jalview2.11, CARA1.9, Sparky3.12, CYANA3.98, TALOS+(web server), CS-Rosetta(web server), AlphaFold2, 3DFSC (web server), Dali (web server)

For manuscripts utilizing custom algorithms or software that are central to the research but not yet described in published literature, software must be made available to editors and reviewers. We strongly encourage code deposition in a community repository (e.g. GitHub). See the Nature Research guidelines for submitting code & software for further information.

Data

Policy information about availability of data

All manuscripts must include a data availability statement. This statement should provide the following information, where applicable:

- Accession codes, unique identifiers, or web links for publicly available datasets
- A list of figures that have associated raw data
- A description of any restrictions on data availability

Cryo-EM density maps have been deposited in the Electron Microscopy Data Bank under accession numbers EMD-26863 (telomerase with CST), EMD-26864 (telomerase with CST–PolαPrim), EMD-26865 (telomerase), EMD-26866 (CST–PolαPrim), EMD-26867 (PolαPrim platform), EMD-26868 (POLA2–POLA1CTD–PRIM2N), and EMD-26869 (PRIM2N–PRIM1). The atomic models have been deposited in the Protein Data Bank under accession codes 7UY5 (telomerase with CST), 7UY6 (telomerase), 7UY7 (CST–PolαPrim), and 7UY8 (PolαPrim platform). Backbone chemical shifts have been deposited in BMRB under accession codes 51441 (Ctc1 OB-A), 51442 (Ctc1 OB-A with p50 peptide 228-250), and 51443 (p50 peptide 228-250).

Field-specific reporting

Please select the one below that is the best fit for your research. If you are not sure, read the appropriate sections before making your selection.

☒ Life sciences ☐ Behavioural & social sciences ☐ Ecological, evolutionary & environmental sciences

For a reference copy of the document with all sections, see nature.com/documents/nr-reporting-summary-flat.pdf

Life sciences study design

All studies must disclose on these points even when the disclosure is negative.

Sample size	No statistical method was used to predetermine sample size. For cryo-EM study, the sample sizes were determined by densities of particles on cryo-EM grids and the number of collected cryo-EM images. 3D reconstructions of telomerase, CST–PolaPrim, and telomerase with CST–PolaPrim were calculated from 36,716 images (~20 million particles). 3D reconstructions of PolaPrim, POLA2–POLA1-CTD–PRIM2n and PRIM2n–PRIM1 were calculated from7,120 images (~3.3 million particles). 2.5 million particles from previously published datasets were combined and used to calculate the 3D reconstruction of telomerase with CST. The data size is comparable to other studies in this field. The number of particles used for each final map is sufficient to obtain reliable classification and reconstruction results by cryo-EM.
Data exclusions	For cryo-EM analysis, particles that do not belong to the class of interest or have poor qualities based on well established cryo-EM principle were excluded after rounds of 2D and 3D classification. This is standard practice required to obtain high resolution cryo-EM structure of the class of interest. For functional studies, no data were excluded from any analysis.
Replication	All biochemical experiments were repeated at least two times and are all reproducible. POLA1–POLA2 and its complex with telomerase were successfully purified three times. POLA1–POLA2–PRIM1–PRIM2 and its complex with telomerase were successfully purified more than ten times. TtCST were successfully purified more than three times for WT and two times for each Ctc1 variant. SEC profiles and protein gels shown in Extended Data Fig. 5a, 5c, 5e, 5f, and 9g present representative results. EMSAs of d(GTTGGG)5 DNA binding by WT and Ctc1 mutant TtCST shown in Fig. 4e and Extended Data Fig. 9i were successfully repeated three times. EMSAs of variant sstDNA binding by WT TtCST shown in Extended Data Fig. 9h were successfully repeated two times. Activity assay results shown in Fig. 3c and Extended Data Fig. 5i-j were successfully repeated three times for each condition.
Randomization	No grouping required for our studies.
Blinding	Blinding was not relevant to this study, because the study does not involve human subjects or live animals and no grouping was conducted for EMSA and activity assays.

Reporting for specific materials, systems and methods

We require information from authors about some types of materials, experimental systems and methods used in many studies. Here, indicate whether each material, system or method listed is relevant to your study. If you are not sure if a list item applies to your research, read the appropriate section before selecting a response.

Materials & experimental systems

n/a	Involved in the study
☒	☐ Antibodies
☐	☒ Eukaryotic cell lines
☒	☐ Palaeontology and archaeology
☒	☐ Animals and other organisms
☒	☐ Human research participants
☒	☐ Clinical data
☒	☐ Dual use research of concern

Methods

n/a	Involved in the study
☒	☐ ChIP-seq
☒	☐ Flow cytometry
☒	☐ MRI-based neuroimaging

Eukaryotic cell lines

Policy information about cell lines

Cell line source(s)	Sf9 cells used for protein expression were purchased from Thermo Fisher Scientific.
Authentication	No authentication was performed.
Mycoplasma contamination	Cells were not tested for mycoplasma contamination.
Commonly misidentified lines (See ICLAC register)	No commonly misidentified lines were used.